DE GRUYTER OPEN

Acta Geophysica
vol. 63, no. 1, Feb. 2015, pp. 62-102
DOI: 10.2478/s11600-014-0206-9

Effect of Stress-Strain Conditions on Physical Precursors and Failure Stages Development in Rock Samples

Kamel BADDARI[1,2,4], Anatoly D. FROLOV[3], Victor TOURTCHINE[4], Fayçal RAHMOUNE[4], and Said MAKDECHE[4]

[1]Laboratory of Physics of the Earth UMBB, Boumerdes, Algeria
e-mail: badari@umbb.dz (corresponding author)
[2]University of Bouira, Bouira, Algeria
[3]Geophysical Division NCG, Russian Academy of Sciences, Moscow, Russia
[4]Laboratory LIMOSE UMBB, Boumerdes, Algeria

Abstract

Precursory stages of failure development in large rock samples were studied and simultaneous observations of the space-time variation of several physical fields were carried out under different stress-strain states. The failure process was studied in detail. A hierarchical structure of discreet rock medium was obtained after loading. It was found that the moisture reduced the rock strength, increased the microcrack distribution and influenced the shape of the failure physical precursors. The rise in temperature up to 400 °C affected the physical precursors at the intermediate and final stages of the failure. Significant variations were detected in the acoustic and electromagnetic emissions. The coalescence criterion was slightly depending on the rock moisture and temperature effect. The possibility of identifying the precursory stage of failure at different strain conditions by means of a complex parameter derived from the convolution of physical recorded data is shown. The obtained results point out the efficiency of the laboratory modelling of seismic processes.

Key words: stress-strain conditions, failure, physical precursor, rock sample.

1. INTRODUCTION

Numerous experiments have been executed in order to understand the process of deformation and the failure of rock samples in relation with the evolution of mechanical instability within the rock masses during geodynamic processes in the earth crust (Benson *et al.* 2007, Heap *et al.* 2011, Bizzari and Cocco 2006, Kuksenko 2005, Lockner *et al*. 1986, Schubnel and Guéguen 2003, Zang *et al.* 2000). Several physical precursors were recorded as the time of rock failure approaches (Adushkin and Turuntaev 2005, Baddari *et al.* 2011, 2012, Darot and Reuschlé 2000, Heap *et al.* 2009, Jouniaux *et al*. 2001, Kadomtsev *et al*. 2011, Cai and Liu 2009, Sobolev 1995). The aim of seismic process experiments modeling in laboratory conditions was to ensure some sort of similarity to natural process (Baddari *et al.* 1996, Brace and Kohlstedt 1980, Glover *et al.* 1996, Jouniaux *et al*. 2006). In most experiments, it has been concluded that variations of electrical resistivity recorded during the process of deformation and fracture of rock samples could be caused by changes of stress, porosity, saturation, and global permeability of the medium (Chen *et al.* 1993, Lockner and Byerlee 1986, Lockner *et al.* 1986, Ponomarev 1987). A number of laboratory observations show that acoustic emission by rock samples in deformation reflects the process of crack genesis and development. The sources and mechanisms of acoustic emission in rock specimens are the growth and closure of microcracks and macrocracks, collapse of pores, twinning processes, motion of dislocations, *etc*. (Lavrov and Shkuratnik 2005). It is known that the process of rock failure is responsible for the reduction in *P* wave velocity that precedes failure in rock. The dilatancy-diffusion earthquake model predicted a decrease and then recovery of V_P/V_S ratio velocity ratio in the epicentral area prior to large earthquakes (Sobolev 1995, Stanchits *et al.* 2003). Indeed, the variations in electrical resistivity and elastic wave velocities could be, to a certain extent, a mirror of the stress-strain state of a rock and the development of heterogeneity in it. Some interesting laboratory results showed the existence of electromagnetic radiation, emitted from loaded rocks (Baddari *et al.* 2011, Bahat *et al.* 2005). The analysis of the obtained results warrants some assumptions on the origin of the registered electromagnetic radiation and the electrical potential difference during the rock failure. The electromagnetic pulses emitted during the nucleation and the expansion of local mechanical instability in the deformed rock volume can be explained by the formation of charged dislocations, electrokinetics phenomena, dislocation and discharge processes, and other physical mechanisms (Baddari *et al*. 2011). It has been suggested that electromagnetic emission can be generated by oscillating dipoles created by ions moving collectively as a surface wave on both faces of the crack (Frid *et al.* 2003, Lacidogna *et al*. 2011), and the electrochemical effects on the boundaries of minerals grains, *etc.* (Soloviev and Spivak

2009). Changes in physico-mechanical state of a rock caused by the rise of cracks concentration areas disrupt the stationary regime. The registered electrical disturbances can be qualitatively explained within the framework of the ions transfer mechanism (Baddari *et al*. 1999, Sobolev 1995), and the electro kinetic effect when water is present (Pozzi and Jouniaux 1994), *etc*. The analyses of some deformation features of rock samples testify that these mechanisms exist, generally, both in dry and moistened conditions.

Besides, the physical precursors of fracture are subject to the impact of numerous factors such as confining loading, pore water pressure and temperature. Fracture under AE feedback and constant strain rate loading were studied in detail by Baddari and Frolov (2010), Lockner and Stanchits (2002), Smirnov and Ponomarev (2004), and Thompson *et al*. (2006). Feedback loading allowed to study in detail the mechanisms of formation and evolution of fracture process. The role of liquid penetration into a stressed rock was investigated by Evans (2005), Kuksenko e*t al.* (2011), Schubnel *et al.* (2007), Shearer (1999), Sobolev and Ponomarev (2011), and Stanchits *et al.* (2003). It is shown that the water initiation into a rock material causes changes in its various physical features (Gupta 2005, Simpson *et al.* 1988, Sobolev and Ponomarev 2011). It should be noted that, as water penetrates into stressed material, the pore pressure increases causing the dilatancy of the rock. It is known that the acoustic emission (AE) due to water infusion into loaded samples is a possible model of swarm seismicity (Smirnov *et al.* 2010, Sobolev *et al*. 2010). The effects of temperature on the physico-mechanical properties of rock samples and the thermal cracking effects on physical rock properties have been studied by Baddari *et al.* (2012), David *et al.* (1999), Fortin *et al.* (2011), Vinciguerra *et al*. (2005), and Wan *et al.* (2009). The thermal cracking effect was also studied by Reuschlé *et al*. (2006). It has been shown that the behavior of rocks under high temperature was different from their behavior at room temperature. Changes in physical and structural rock properties have been obtained under an increased temperature. At room temperature, rock is generally in brittle failure mode. Changes in elastic modulus, Poissons's ratio, thermal expansion coefficient, and structural chemical reactions have been obtained with the temperature increase. The influence of temperature on various rocks parameters differs from one rock to another. Young's modulus, for example, for rocks like andesite, granite and quartz trachyte, gradually decreased about 20-30% along with a temperature increasing from 20 to 600 °C. Very weak changes have been recorded for the elastic modulus as the temperature increased over 300 °C for rocks like tuft and pottery stone (Xu *et al.* 2008, Zhang *et al.* 2009).

Currently, the problematic of extrapolating laboratory results to nature meets a number of difficulties associated both with technology and methods.

The matter concerns the reliability of the obtained precursors, their universality and the precision of their skill determination**.**

The present work describes the effect of strain-stress conditions on rock macrofailure formation. The use of different large rock samples in our tests permits to explorer the universality of the physical precursors of failure whatever the type of rock, the monitoring of several parameters simultaneously, the differential properties of rocks, the distribution of different physical parameters over the rock volume with using various pick-ups attached to the sample and the failure due to accumulation in the rock volume of elastic deformation. The laboratory experiments carried out in the present work address the study of the effect of stress-strain conditions on the process of rock failure and some spatial resolution of the precursory behavior under various deformation conditions. For this purpose, we analyze the deformation to failure observations on large rock samples in five types of experiments:

I The deformation of dry samples under action of controlled biaxial stress.

II The deformation of moistened samples under controlled biaxal loading.

III The deformation of samples during the variation of strain regime, when the vertical load P was stabilized constant at the stage (0.8 to 0.9) t/t_f and the horizontal load H decreased up to zero.

IV The deformation of samples under conditions of uniaxial load and relatively high strain rate (10^{-6} s^{-1}).

V The deformation of samples under controlled uniaxial load and various temperatures.

Interest of these experiments concerns the fact that a large number of factors affects rock massif in the earth crust conditions, such as mechanical instability, pressure impact, moisture, temperature, *etc*. In order to reinforce our approach, a multi statistical analysis has been applied to summarize information on series of physical failure precursors of a strained rock, which allows to identify a macrofailure precursor by means of a complex parameter.

2. EXPERIMENTAL METHODOLOGY

2.1 Rock samples and deformation apparatus

Large rock samples have been submitted to a series of independent laboratory experiments. Samples of granite, marble, diabase, pyrophyllite and concrete were shaped as a rectangular parallelepiped $450 \times 450 \times 350$ mm in size. Two pairs of glass plates, acting as stress concentrators, of dimensions of $150 \times 150 \times 7$ mm, have been inserted within the sample under an angle of 40° in relation to the vertical axis of the pattern, in order to favor the shear-

ing rupture (Fig. 1). This laboratory simulation can be regarded as a simplified model of the seismic gap process development.

A petrographic analysis gave compositions as follows. The granite contained 42% of albite, 42% of quartz, 39% of biotite, and admixture of muscovite, pyrite and other components, the grain size was 1-2 mm, the density 2.7 g/cm^3, the bulk porosity 2.3%. The marble contained 96% of calcite, 2.5% of dolomite, and 1.5% of other minerals, the grain size was 0.07-1.5 mm, the density 2.7 g/cm^3, the bulk porosity 0.34%. The diabase contained 60% of plagioclase, 20% of olivine, 10% of monocline pyroxene, and 10% of augite, diopside, ilmenite, and apatite, the grain size was less than 1.5 mm, and the bulk porosity was 6%. The sample of pyrophyllite contained more of 45% of silicates of aluminum, the density was 2.7 g/cm^3, the bulk porosity 5%. The concrete sample was prepared out of cement 25%, quartz sand 20%, fine-grained granite 48%, and water 10%.

A servo controlled and AE rate feedback press was used to load rock samples. The apparatus was equipped with a load and a displacement meas-

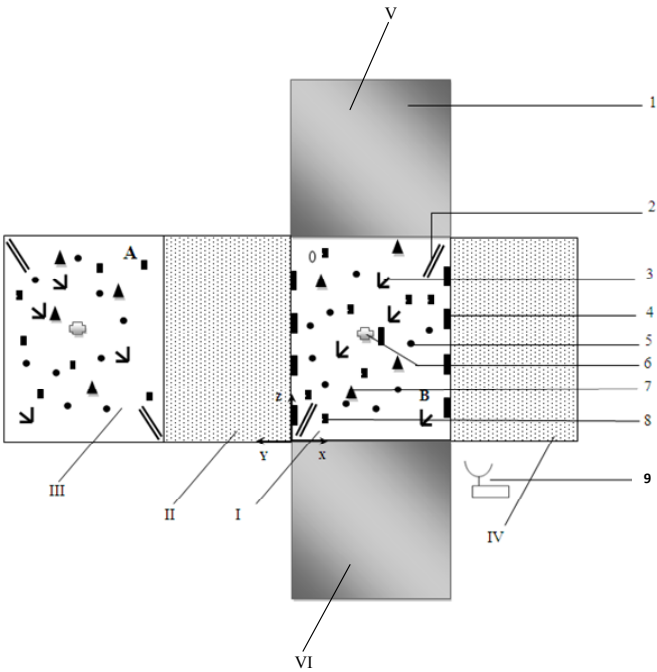

Fig. 1. Schematic diagram of the experiment arrangement. 1 – rock sample; 2 – artificial stress concentrator; 3 – strain rosette; 4 – AE transducer; 5 – elastic wave sound; 6 – thermal sensor; 7 – pick-up electric resistivity electrode; A, B – feeding electrodes; 0 – zero electrode; 8 – self potential electrode; 9 – antenna. I – VI: faces of the sample.

uring systems. The deformation apparatus was linked to a computer-controlled loading in order to measure and maintain the loading force, the preset load rate, the mobile clamp displacement and to record the experimental results. The program system was developed as a programmable feedback controller**.** A transducer was fixed in the middle part of the sample in order to provide feedback for controlling the loading rate as a function of the acoustic activity. The particular load regime has an inverse coupling with AE: with the increase of this latter, the speed of loading is diminished. A feedback between an AE pulse counter and the axial stress ensured a constant AE velocity throughout the trial. The AE activity used in the chain of the inverse command corresponded to the first dozens of events per second. AE rate growth conducted immediately to a decrease in the axial load by the reduction of the motion speed of the piston pressure, making it possible to monitor the failure process under quasi-static conditions. The considerate strain control regime was selected in accordance with the notion relative to the process occurring in the earthquake focal zones. The axial load was measured at the rate of 1s intervals on a PC. Experimental equipment and techniques were described in details in our previous work (Baddari *et al.* 2011, 2012). Laboratory experiments using the inverse loading technique by acoustic emission enabled us to extend the final phase of source development and analyze in details the acoustic regime (Baddari and Frolov 2010, Dresen *et al.* 2010, Lockner *et al*. 1991, Smirnov *et al*. 2010).

2.2 The experiments

Experiments were executed under five strain conditions. The deformation of dry samples under action of controlled biaxial stress has been executed in conditions of a variable vertical load P, and a constant (75 MPa) horizontal load H. Three cycles of stress variation are identified in mean load P as follows: 1 – growth to close to maximum values P_{max} in the interval $(0\text{-}0.45)t/t_f$, where t is the experimental current time, named with respect to a total lifetime t_f of experiment; 2 – constant stress up to $(0.75\text{-}0.8)t/t_f$; 3 – drop of stress due to macrofailure initiation in the interval $[(0.75\text{-}0.8) - 1]t/t_f$. The loading has been realized in the condition of invariability of the AE intensity.

In order to study the role of pore water in the development of failure, similar samples, but sutured with water were deformed under action of controlled biaxial load used in the previous experiment. After drying to constant weight by heating the rock samples at $T°$= 110-130 °C and the air was removed from pores, the samples were placed in water basin in a vacuum chamber during 60 days. The maximum moisture absorption was characterized by constant sample weight. The total saturation corresponded to 0.3-5% moisture content, depending on porosity of each rock sample.

To study the effect of strain regime, the vertical load P was stabilized constant at stage (0.8 to 0.9)t/t_f and the horizontal load H decreased up to zero. Samples similar to that used in previous tests were loaded under conditions of uniaxial load and relatively high strain rate (10^{-6} s^{-1}).

Finally, the same samples were deformed under controlled uniaxial load and various temperatures. In these last experiments, the samples were heated and kept at a given temperature, until the rupture was carried out, by means of a high temperature furnace formed by bifacial heat transmitter. Each sample was heated by an imposed temperature mechanism on two opposite sides at a temperature rate of 2 °C. The temperature was maintained constant during 2.5-3.5 hours, and then the sample was heated from outside, until reaching the selected temperature on the two free sides, where thermal sensors were cemented in order to measure the temperature in the sample under study. Measurements of mechanical, acoustic, and electrical parameters were carried out in the intervals of selected temperatures: 100, 200, 300, and 400°C. Experimental equipment and techniques of the influence of temperature on the kinetics of the deformation, and the rock rupture process were described and discussed in details by Baddari *et al.* (2012).

2.3 Data acquisition and data processing

We have studied the local strain field, acoustic and electromagnetic emissions, and characteristics of elastic waves by means of ultrasonic monitoring, the own electrical polarization and the electrical resistivity (Fig. 1).

A system of three rosettes was fixed right on the line connecting the stress concentrators, *i.e.*, in the route of the main failure and the fourth rosette in the stable area unaffected by the macrofailure. The relative strain readings were measured from vertical ε_z and horizontal ε_x strain components. The first tensor invariant of the plane strain $\Im = \varepsilon_z + \varepsilon_x$ was computed with an absolute error of 5×10^{-5}.

Acoustic signals were received by eight of 10 mm diameter, 1 mm-wide piezoelectric transducers (PZT) of eigenfrequency of 0.2 MHz. The sensors were linked to input amplifiers, oscillographs GRS-6052, and computer. The acoustic events recording was carried out in numerical form of the time of the first arrivals and the amplitudes of the first maxima of signals. The numerical channel resolution for the determination of the arrival time was of 0.05 μs. To pinpoint AE sources, a seismological algorithm (Baddari *et al.* 2011, Smirnov *et al.* 2010) has been used to locate hypocenter coordinates by the difference in AE signals registration time. The acoustic events having a travel time higher than 5 μs were eliminated from the AE catalogue. The uncertainty in determining the hypocenters coordinates was of 1-1.5 mm, according to the acoustic event value. The AE catalogue was composed by the Cartesian coordinates, the time, and the energy class C ($C = 2 \lg A$, where A

is the amplitude of the pulse in mV brought back to a distance of 10 mm from the hypocenter; A^2 is proportional to the energy of the event). Parameter C in this case is similar to the energy class used in seismology. The calculations have been realised in windows of 1000 events and varying by a step of 500.

The electromagnetic emission (EMR) monitoring was performed using a unit of three magnetic antennas of different magnetic permeability of low, mid, and high frequencies, located near the lateral surface of the sample at 0.5 m. The experimental technique and methodology were described in our previous work (Baddari *et al.* 2011). The received signals that occurred in the rock sample as it was deformed were amplified and processed in a formation block. Regular frequency characteristics of the signal reception chain in a tuning fork varied from 400 Hz to 3 MHz. These signals were passed through a quadratic amplitude detector, from which the processed signal arrived to the block of analogue memory where its maximum amplitude was stored in an interval of 10 μs. At the end of this period, a rectangular pulse of positive polarisation of duration of 2-3 μs was formed at the output of an electronic switch. Then, this pulse was directed to the analyser *H*/024-07 in order to obtain the energetic spectra of EMR. To eliminate disturbances on the energetic spectrum, an adjusted compensatory antenna was installed 2 m away from the rock sample in its controlled area. The received signals by this antenna were amplified and compared to the threshold of the triggering off the installation reserved to produce an electric potential for the command block. If the signal from this antenna exceeds a certain level, the command block was blocked and did not transmit signals to the electronic switch, so the undesired signals did not arrive at the input of the pulse analyser. Finally, the investigated frequency range was from first kHz up to 2 MHz.

The ultrasonic wave velocity was determined by compressional transducers with a free resonance frequency from 80 to 100 kHz and $10 \times 10 \times 10$ mm size. The records equipment included a GS13 pulse generator, SP5022 seismoscope, 7402FM frequency meter, GRS6052 oscillograph, and PC. The transducers were used as radiators and detectors of ultrasonic signals. Mainly *P*-wave sensors were used, but these can easily be replaced by *S*-wave ones. Ultrasonic monitoring started under no-load conditions, but as cycled loading progressed, series of measurements along the routes were taken. The arrival time of the first break was used to calculate the ultrasonic velocities. The sensors were fixed on the faces of samples and the number of monitored ray paths was 30; enabling to study velocity variations in measuring *P*- and *S*-wave arrival times with an accuracy of about 0.7%. The elastic wave velocities have been measured following the ultrasound traces under angles of 45° with respect to the side *I* of rock sample allowing to record *P*- and *S*-waves.

The electrical field was measured by nonpolarizable silver chloride electrodes enclosed in special holders, which were mounted on the free faces of the specimen. Their potential stability did not exceed 0.1-0.2 mV. Silver chloride electrodes were used as supply electrodes, both tapping off the 2 V power source. Rock samples were polarized during 30 s. After the current interruption by the disconnection of the power source, the electric potential was registered. Different combinations of pick-offs served as receiving pairs of electrodes MN and enabled to study the structure of the electrical potential in detail. Measurements were taken regularly every 1-2 min. The background values had been estimated prior to the experiment by carrying out an aerial survey of surface potentials on a 2×2 cm grid on all free faces of the specimen. As a result, it was possible to detect changes of the order of 1 mV and less in the self potentials.

The apparent electrical resistivity monitoring was studied using direct current and electrode devices in different orientations. Various combinations of the nonpolarizable sensors acted as dipoles. The feeding graphite electrodes, diameter in 2 and 1 mm thick, were attached on free surfaces of the rock sample. A stabilized current to 0.01% has been injected through these electrodes. While waiting 30 s, the measurements started when the polarization effect dropped to 0.5% of a measured value. Measurements in continuous and automatic regime of the apparent electrical resistivity were realized at an electrode pairs. It should be noted that the measurements realized during ten days in unloaded samples showed constancy in electric parameter measurements down to 0.5-2% precision. The methodology enabled us to evaluate relative changes of resistivity both in the entire sample and in separate parts of it. Dozens of electric surveys were conducted during loading cycle. The apparent resistivity was obtained using the formula $\Delta\rho_a = (\rho_t - \rho_0)/\rho_0$, where ρ_0 is the value of ρ_a before containment, and ρ_t is the value of ρ_a at the time t. In all cases, the used technical methods and continuous measurements insured high sensitivity and reliability of the apparent electrical resistivity parameter. Similar technical methodology of electrical parameters measurement was used by Baddari *et al*. (1999, 2012), Ponomarev (1987), and Sobolev (1995).

3. RESULTS

3.1 Defect accumulation and hierarchical failure process in dry samples

Structural discontinuity of rock massif in the earth crust is due to seismogenic and volcanic activities (Ammon *et al.* 2008, Kuksenko *et al.* 2011, Shearer 1999). Microscopic examination of sections of samples and thin plates, after experiments using dry samples, was used to study the specificity of the failure in each deformed rock. For samples of granite, diabase, and pyrophyllite,

Fig. 2. Schema of the location of cracks in rock samples after the experiments in dry strain conditions: granite (a), marble (b), diabase (c), pyrophyllite (d), and concrete (e).

we noticed cracks systems of h 0.1-0.2 mm length with a dominant orientation angles in the range of 30-45° and 55-60° with respect to the vertical stress P. Short subparallel cracks oriented under angles of 20-35° in relation to the main crack were observed in the diabase and pyrophyllite. Marble sample showed shear failures under an angle of 35-60°. The main macrofailure was a result of formation of subparallel system of microcracks in the granite and diabase samples. Microcracks were oriented under angles of

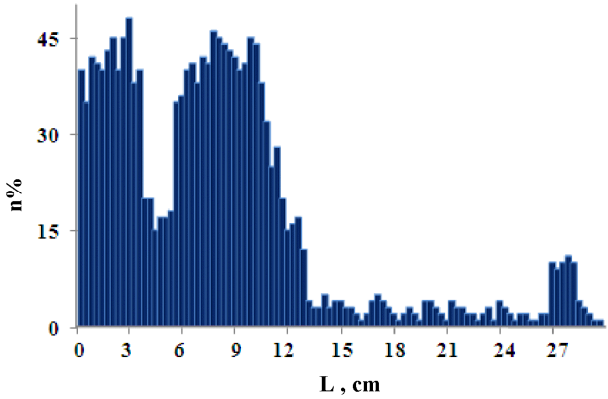

Fig. 3. Histogram of mean geometric size distribution of adjacent failures in diabase sample.

30 to 50° in the concrete sample. Figure 2 gives schemes of observed, according to a visual examination, of macrocracks in all samples after the experiments. It shows a blocky hierarchical formation. The ratio of two basic adjacent sizes, for all samples, during and after experiments, gave $L_i/L_{i-1} = \beta = 10^{\alpha}$, where $\beta = 2.5\text{-}3.5$ and $\alpha = 0.01\text{-}0.08$. Figure 3 shows, as an example, a diagram of mean geometric size distribution of adjacent failures in diabase sample. The histogram shows three maxima and the ratio of adjacent blocks mean sizes is in the order of 3. Similar results have been obtained by Asatryan *et al.* (1993). This structural discreteness reminds that after a seismic shock or anthropogenic activity, the continuity of rock massif is an object of considerable heterogeneity of faults, inter-block contacts and various fractures, which will act as stress concentrators under the action of natural stresses. This testifies to the self-similarity of failure process at different scale levels in agreement with Baddari and Frolov (2010), Sadovsky *et al.* (1991), Sobolev (1995) that binds the rupture process structure in the geophysical field to some characteristic sizes.

Acoustic and electromagnetic emissions produced in the process of deformation and failure were used in studying the redistribution of cracks in the fracture process accumulation. As an example, Fig. 4a shows changes in the number of acoustic events for the macrofailure zone in the granite obtained between the stress concentrators at different strain-stress stages. We note a gradual rise in the number of acoustic signals reaching its peak before the failure. The projection of the AE coordinates allows to reveal three characteristic stages of the focus genesis. Stage I corresponds to the formation of independent dispersed microcracks in the volume rock sample. The size of cracks at this stage is of the order of those grains (Sobolev and Ponomarev 2003). Characteristic microcracks dimensions corresponding to the mini-

mum acoustic signals amplitudes of 8-10 mV was about 70-90 μ in concordance with the results obtained by Baddari *et al*. (2011) and Ponomarev *et al.* (1997). Microscopic measurements gave approximately the same lengths.

(a)

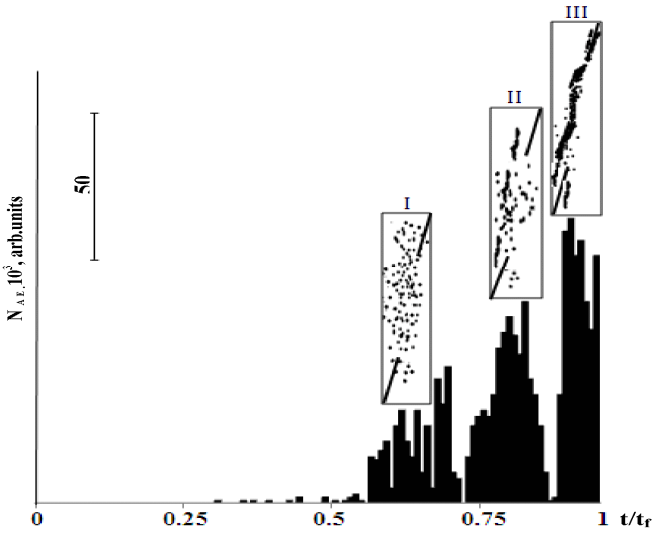

(b)

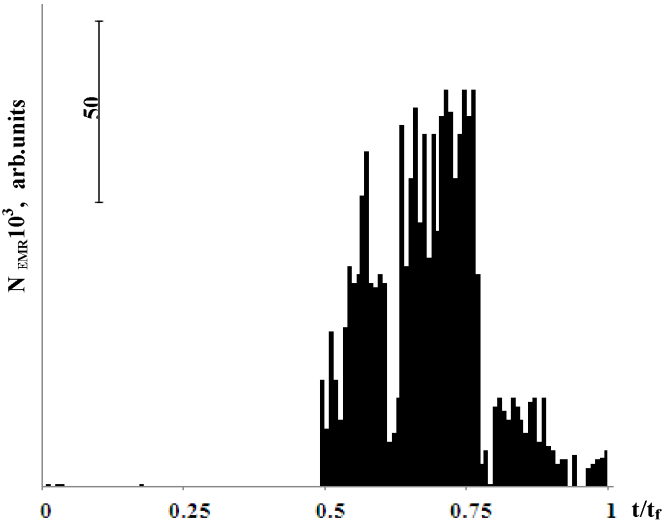

Fig. 4: (a) Energy released spectra of AE during the deformation of granite sample. Schemes of cracks hypocenters are shown above the plot. I – III – three stress-strain stages process; (b) Typical record of the total added released EMR energy in diabase sample.

It should be noted that the size of cracks emitting the lowest acoustic signals is calculated by the formula (Baddari *et al*. 1996, Ponomarev *et al.* 1997): $l_i = \beta A^{2/3}$, where A is the signal amplitude and β is a constant. The minimum amplitudes of the AE recorded during our tests were 8-10 mV. Stage II corresponds to an increasing accumulation of microcracks leading to their concentration and the formation of close microcracks sets able to interact and unify. The latter gave rise to defects with dimensions by an order of magnitude larger. Stage III is characterized by a localization of the main failure focus, which will develop the macrofailure. Figure 4a shows two acoustic quiescence periods at 0.71 and 0.9 [t/t_f], corresponding to the scenario preceding the respective transition from lower ($i - 1$) to higher (i) and from (i) to ($i + 1$) levels of cracking hierarchy. Using the formula

$$\log l_i = a \log E + b \,, \tag{1}$$

with $a \approx 0.25$, we can deduce that the variation of the energy E of an order of magnitude induced a twofold increase in the length l_i of the crack (Baddari *et al*. 2011, Sobolev and Ponomarev 2003). The decay in acoustic activity at each loading step obeys generally the Omori law (Lavrov and Shkuratnik 2005, Lockner 1993, Rudajev *et al.* 1996, Smirnov and Ponomarev 2004, Utsu 2002)

$$\Delta n / \Delta t = A_0 (t + c)^{-p} \,, \tag{2}$$

where A_0 is the initial number of acoustic signals in a time unit, c and p are constant values, and t denotes the time. An estimate of $0.55 \leq p \leq 2.0$ for values of p has been obtained. Utsu *et al.* (1995) obtained $0.6 \leq p \leq 2.5$ in relation with aftershock activity. Note that A_0 increases and the parameter p decreases prior to the progressive macrofailure. The decrease in p can be understood as a prediction criterion of the expected rock instability.

The experiments show that the EMR amplitude A changed from 10 to 120 mV. Figure 4b gives a typical record of the total added released energy summed up in 100 s interval of EMR in the stress concentrators zone of the diabase sample. The energy of an electromagnetic event was estimated from the amplitude of the first maximum of a signal. The first phase, corresponding to a gradual rise in differential loading, is characterized by a low intensity of EMR events, which begin to be recorded at the end of this phase at $t/t_f = 0.48$-0.5, and reflects the beginning of weak microcracks process. The stage from 0.49 to 0.78 [t/t_f] is marked by numerous minor cracks accumulation and is characterized by rising EMR intensity. The non-uniformity of this intensity reflects the relaxation character in the variation of the stress concentration in the sample which has been shared in robust and fragile zones. At the time of loading $t/t_f = 0.78$-0.9, the EMR variations decreased reflecting a gradual concentration of cracks around an incipient macrofailure. The

last phase 0.9-1 [t/t_f] unfolds against a falling EMR and the main fault taking shape. The dynamic of increase and relaxation of EMR, in our opinion, reflects the growth and closure of microcracks, and dislocations motion at grains boundaries and grains contacts in the rock body. The generation of minor cracks gives rise to high frequency EMR signals of no less 10-15 μs duration and more than 300 kHz base frequency; however their fusion upon reaching a critical concentration leads to low frequency EMR pulses (10-20 kHz) and 150-350 μs duration. We noticed a gradual increase in the amount of the last signals about 40-60 min prior the main shock triggering.

The analysis of registered EMR pulses allowed to classify arbitrarily the EMR energy into three classes: $C_1 = 1.2\text{-}2.2$, $C_2 = 2.2\text{-}2.8$, and $C_3 \geq 2.8$, which correspond to three sizes of cracks l_1, l_2, and l_3 (Eq. 1). Three classes were selected according to the recorded number of electromagnetic signals N_1, N_2, and N_3, respectively. Figure 5 shows an example of the variation of EMR for the three classes $C_1 - C_3$ in the experiment with the pyrophyllite. It gives the curve of loading and the number of EMR pulses per unit of time N, normalized to their ultimate values. We noted that phases of EMR evolution have been maintained. The EMR showed an electromagnetic quiescence more visible and longer for C_2 and C_3 at $t/t_f = 0.94\text{-}1$ and at $t/t_f = 0.96\text{-}1$, respectively (Fig. 5b, c). An electromagnetic quiescence is likely to occur only under a definite relationship between energies of registered minor shocks viewed as a background for the impending macroshock.

The possible physical explanation of the delocalized failure ultimate concentration can be based on the equation of the solid state strength kinetic theory (Kuksenko 2005, Sobolev 1995, Zhurkov 1984)

$$t = t_0 \, e^{(E_0 - \gamma\sigma)/kT} , \tag{3}$$

where E_0 is the failure activation energy, close in value to interatomic bond energy, k is the Boltzmann constant, t_0 is the pre-exponential factor with value equaling that of solid state atoms heat fluctuation period, and γ is a structurally sensitive parameter defining local overstresses. Equation 3 expresses the relationship revealed between the lifetime t, the tensile stress σ, and absolute temperature T. For the case of a constant temperature, Eq. 3 may be transformed to a simpler relation for the lifetime

$$t = B \, e^{-\alpha\sigma} , \tag{4}$$

where $B = t_0 \, e^{U_0/kT}$ and $\alpha = \gamma/kT$. By analogy to the kinetic equation, it is possible to assume that the rate of crack accumulation dN/dt can be defined as follows:

$$dN / dt = (dN / dt)_0 e^{(E_0 - \gamma\sigma)/kT} , \tag{5}$$

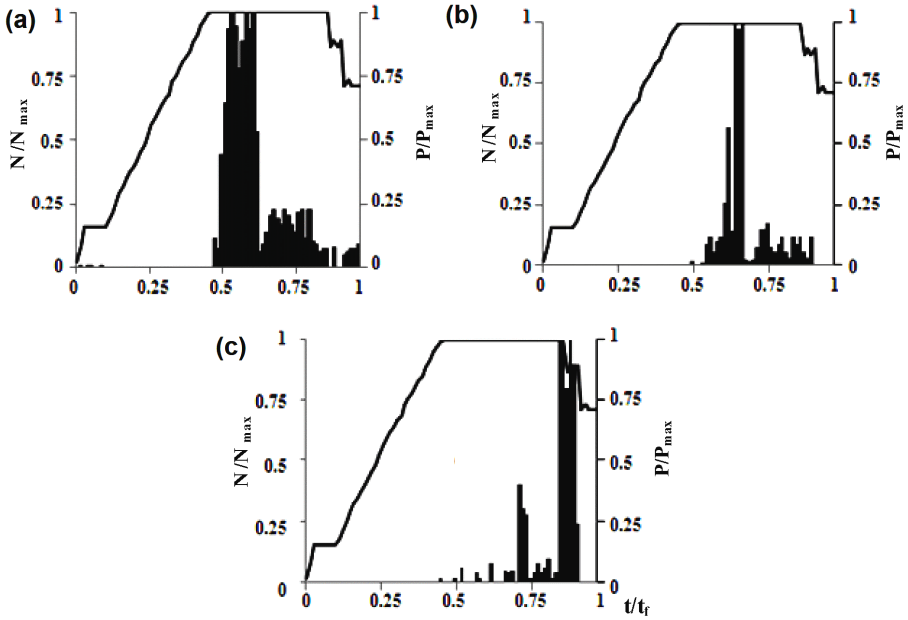

Fig. 5. Variations of EMR for energetic classes: (a) C_1, (b) C_2, and (c) C_3 in pyrophyllite sample. N/N_{max} and P/P_{max} represent the number of EMR pulses per unit of time N and the load P normalized to their ultimate values respectively.

which testifies that the process of kinetics of crack accumulation determines the lifetime t of a stressed rock which is made up of the duration stage deformation t_i and that t_s of a failure source rise $t = t_i + t_s$, with $t_s < t_i$. The failure focus rise is a result of the microcracking transition from delocalisation to localisation, and consequently changes in the physical subsystems structure of rock material. The associated physical subsystems, conditioning the response to external mechanical influences, are ionic, dipolar, and electronic holes. The changes in the spatial structure are accompanied by some changes in mechanical, electrical, and other physical properties of the medium, most of which can be recorded by remote sensing methods.

Results of experimental investigations of failure show that structures cracks sets obey the fractal statistics (Baddari *et al.* 2011, 2012; Sobolev 1995, Zavyalov 2006, Zhurkov *et al.* 1980). In a chaotic distribution of microcracks, the probability of the formation of a set of x adjacent cracks, *i.e.*, the transition from delocalization to localization, is

$$p_n = \frac{\langle x \rangle^x}{x!} \tag{6}$$

with the mean number $\langle x \rangle$ of cracks by cluster equal to $\langle x \rangle = x/K$ and the mean inter-crack distance K during their volumetric concentration per unit of size $N = xV^{-1}$ equal to

$$K = N^{-1/3} / \overline{l} \,, \tag{7}$$

where V is the volume of the confined rock, and $\overline{l}$ is the mean size of the accumulated cracks given by

$$\overline{l} = \frac{1}{x} \sum_{i=1}^{x} l_i \tag{8}$$

with l_i the size of the crack. Equation 6 reminds the Poisson formula without the multiple $e^{-\langle x \rangle}$. The use of the formula of Sterling for the factorial of a large number $x >> 1$ in Eq. 6 leads to

$$(2\pi x)^{1/2} x^x e^{-x} \le x! \le (2\pi x)^{1/2} x^x e^{-x} \left(1 + (12x)^{-1}\right). \tag{9}$$

As $\sum_{x=1}^{\infty} p_x = 1$, in the case of a dense set fluctuation, we have

$$(2\pi)^{-1/2} \le \sum_{x=1}^{\infty} \left(\frac{e}{K}\right)^x \tag{10}$$

and the criterion of clustering cracks to generate a quick failure of the rock is

$$K \le e\left(1 + (2\pi)^{-1/2}\right). \tag{11}$$

The absolute error ΔK is $\Delta K \le 0.5 \ 10^{i-j+1}$ with $i - j + 1 = -8$ and consequently the exact value of the calescence criterion is $K^* = 3.8$, which constitutes the threshold of the transition from the stage of crack accumulation to their start to coalesce and the formation ensembles of clusters in the cracked body.

Since we did not measure the crack size l_i (Eq. 8) during the experiments, the methodology explained in Baddari *et al*. (2012), Smirnov *et al.* (1995) has been used, and therefore

$$K = x^{2/3} V^{1/3} \Big/ \beta \sum_{i=1}^{x} A_i^{2/3} \,, \tag{12}$$

where A_i is the amplitude of the acoustic signal and β is a constant, evaluated empirically equal to 0.2 mm/mV$^{2/3}$.

The location of the failure was controlled by the Pearson criterion

$$\chi = (N_i - x_i)^2 / (x_i)^2 \,, \tag{13}$$

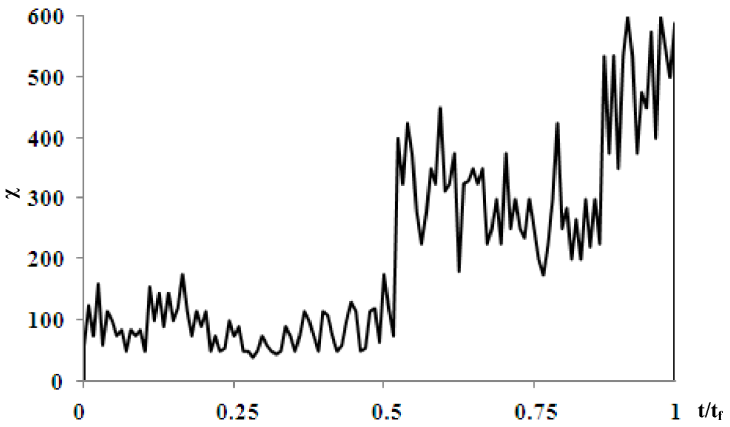

Fig. 6. Variation of the Pearson criterion during the deformation of concrete sample.

where x_i is the number of cracks in the sample unit volumes for an uniform distribution of acoustic signals, *i.e.*, received signals in the specified amplitudes range $A + dA$, and N_i the real number of signals in these volumes, *i.e.*, all emitted signals. The log$A$ values were divided into ten categories and the number of signals was calculated for each category. As a typical example Fig. 6 shows the variation of χ for the deformed sample in experiment with the concrete. The value of χ remained almost constant until $t = 0.5$ $[t/t_f]$ and then increased sharply up to $t = 0.8$ $[t/t_f]$, which indicated the location of AE. A second growth is recorded from $t = 0.9$ $[t/t_f]$ until the end of the test, which confirms the hierarchical progression of the failure. The stochastic nature of the EA has been preserved.

3.2 Parameters of physical fields in deformed dry samples under a strain control regime

Experimental data have yielded a series of stable variations in physical parameters depending on the strain-stress state of the rock. Figure 7 shows the experimental results with dry samples. In this case, the samples have been heated in kilns at temperatures of 110-130 °C until they reached constant weight. Figure 7 Ia shows the variation of the first flat strain tensor invariant $\mathcal{J}$ for rosette situated in the affected area by the macrocrack. We can identify three stages of deformation illustrating the different stages of the deformation process evolution. The first stage, A, from 0 to 0.5 $[t/t_f]$ corresponded to the stage of separate stable microscopic cracks accumulation in the entire solid body. The second one, B, was characterized by a relative slowdown in growth of $\mathcal{J}$ and its transition by an extremum. It has been observed in the area of maximal stresses corresponded to the irreversible rock deformation.

It has been characterized by microcracks growth process and the beginning of their mutual interaction triggering finally a macrofailure nucleus in the area of an incipient macrofailure. The final stage, *C*, characterized by negative deviations from the X-axis, unfolded during the step of failing stress while the macrofailure nucleus increased and the main fault was shaped.

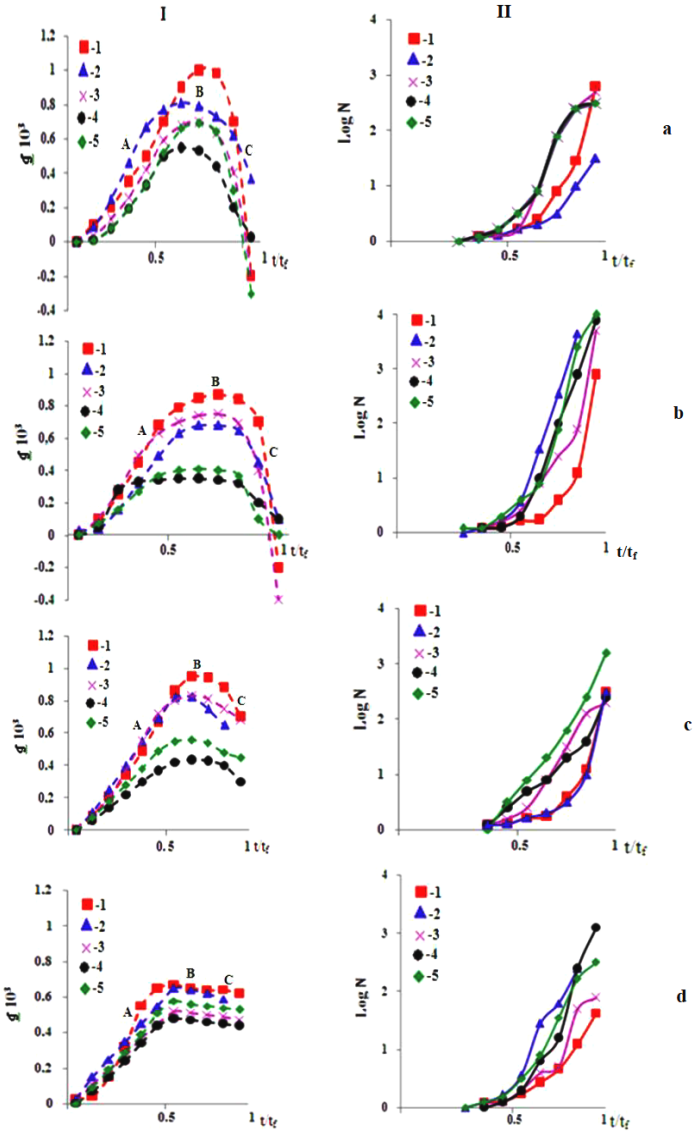

Fig. 7. Continued on next page.

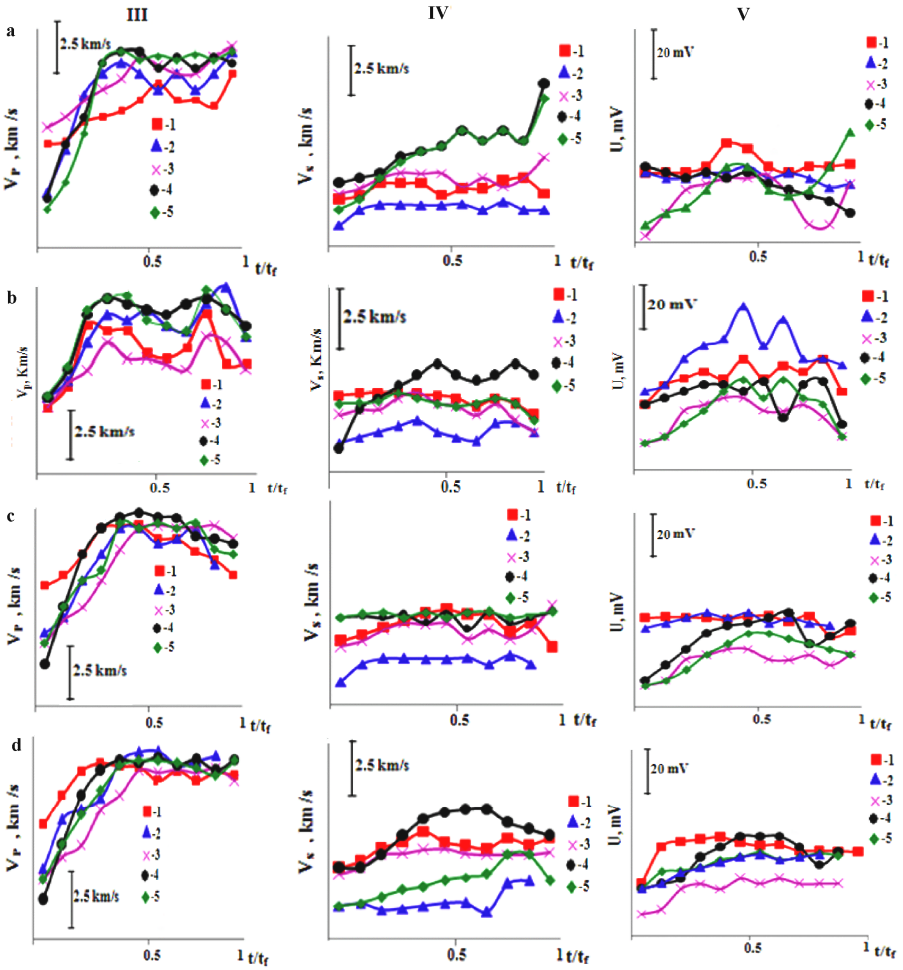

Fig. 7. Variations of physical parameters during the deformation and the failure rock samples under various strain conditions: dry samples (a), moistened samples (b), variation of the strain regime (c), and deformation at high strain rate (d). 1 – granite, 2 – marble, 3 – diabase, 4 – pyrophyllite,5 – concrete. I – first tensor invariant of flat deformation, II – AE intensity N, III – V_P, IV – V_S, V – electrical potential ΔU.

It should be noted that the positive deviations of $\mathcal{J}$ from the X-axis point to the element square contraction, while negative – dilatancy (Baddari *et al.* 2012, Sobolev 1995).

The initial stage (up to 0.4-0.5 t/t_f) is characterized, generally, by low activity of the AE received by all the transducers (Fig. 7 IIa), strong increase of V_P and low variation of V_S for routes situated along the macrofailure path

(Fig. 7 III-IVa), and a constant or negligible variation of the electrical potential ΔU for the pyrophyllite and concrete samples, and growth of this latter for diabase and marble samples. A slight increase of ΔU was noted for the granite at the end of this stage (Fig. 7 Va). These changes are uniform across the sample. This step corresponds to a material sample consolidation and the beginning of microcracking. This stage is characterized by the extensively nonuniform and isolated spatial distribution of microcracks. The second stage of the sample deformation (0.5-0.8 t/t_f) is characterized by a growth of the AE for all samples, bay – shaped oscillations, and drops in variations of V_P and V_S, which accompanied the dilatancy, the decrease of ΔU for granite, diabase, pyrophyllite, concrete, and a decrease followed by growth of this latter for the marble. An increase by intervals in the activity of the AE was observed. This step corresponded to an intense sample micofissuration. The third stage (over 0.8-0.85 t/t_f), characterized by a slow deformation of the sample, is accompanied by sudden increases of the AE for all samples, increases for granite, marble, diabase, and concrete samples, during the last phase of this stage (0.9-1 t/t_f) in V_P, a decrease of V_P for the pyrophyllite, increases of V_S for the diabase, pyrophyllite, and concrete samples, a decrease of V_S for the granite and its negligible variations for the marble. This deformation stage has increased ΔU in the marble, diabase, concrete and granite during the last step. Drop in ΔU was recorded for the pyrophyllite just before the end of the test. The analysis of the distribution of acoustic signals showed a cluster of AE hypocenters, which testifies to a step of the progressive macrofailure and the beginning disintegration phase in the rock material. We noted a dispersion of V_P and V_S velocities for the second and third stages caused probably by the increase volume of inhomogeneity and anisotropy due to the fracturing propagation, tensile, shears and various structural damages in stressed sample. An important elastic anisotropy was developed prior to failure, which was due to oriented microcracks, their concentration and their distribution pattern. The mean square velocity δ deviation determined for 15 routes shows that the increase in stress is accompanied by increased velocities scatter (Fig. 8). The failure occurred differently in the different zones of intersection of theses paths. Figure 8 demonstrates, as an indication, the behavior of the ratio V_P/V_S velocities variations for sets of elements 1-3 and 2-4 situated along and across the stress-concentrators, respectively in a granite sample. The behavior of the V_P/V_S ratio through the trace 2-4 was antagonistic that 1-3, which reflected the anisotropy of strength and the distribution of mechanical stresses in deformed rock sample. Roughly similar graphs were obtained for the other rock sample. It has been noted that the dynamics of cracking structure formation is more active in the vertical direction than in the horizontal one for all rocks. The ratio V_P/V_S

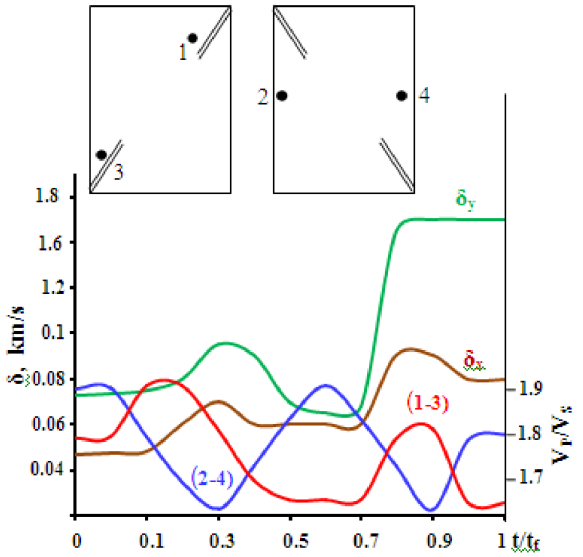

Fig. 8. V_P/V_S ratio observed in macrofailure area for routes 1-3 and 2-4. σ_y and σ_x are the mean square velocities computed according to the vertical Y and horizontal X-axis of the granite sample.

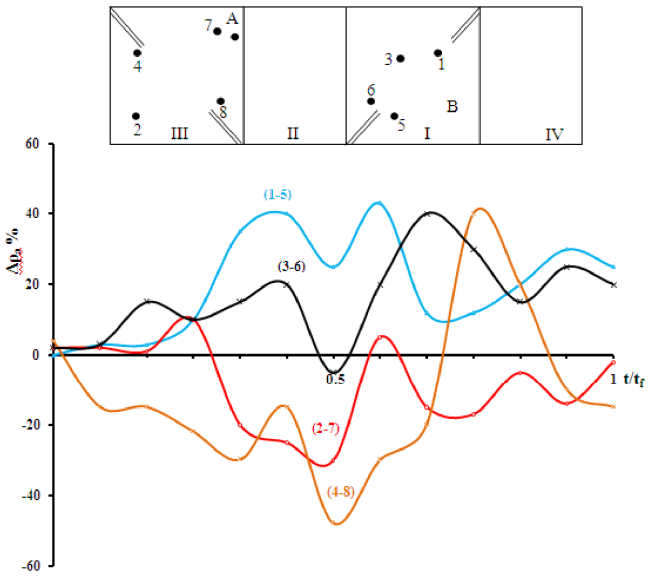

Fig. 9. Typical anisotropy registered in electrical resistivity measured for different positions of pick-up electrode pairs in granite sample. Scheme of four (I-IV) sample facets with the introduced stress concentrators, pick-up electrodes: 1, 2, 3, 4, 5, 6, 7, and feeding electrodes A, B are shown above the plot.

showed a negligible change in the stable zones for all samples. Similar, on the whole, results have been obtained in our previous work (Baddari and Frolov 2010). Anisotropy in $\Delta\rho_a$ was recorded during the half of the first stage of deformation between 0.3 and 0.5 [t/t_f], the second anisotropy at (0.6-0.8)t/t_f and last one at (0.8-1)t/t_f of rock failure (Fig. 9). A bay variation of $\Delta\rho_a$ has been obtained in the routes passing through the jumper center between the stress concentrators in the experiment with the granite sample. The bay's reversal was recorded in perpendicular routes. The increase of $\Delta\rho_a$ in perpendicular direction is probably caused by coalescing oriented cracks and rupture of conducting paths system during the macrocrack formation. Similar anisotropies in $\Delta\rho_a$ were recorded for all tested rocks.

3.3 Influence of various factors on the physical precursors

3.3.1 Influence of moisture

Moisture extended the second strain stage B recorded in the parameter $\mathcal{J}$ (Fig. 7 Ib). The trend of the AE was affected by moisture (Fig. 7 IIb). We noted more intense AE activity for the moistened rocks. The V_P and V_S velocities marked a sensible drop during the second stage of rock deformation at 0.4-0.65 t/t_f. Some anomalies were found in the variations of longitudinal V_P and transversal V_S wave velocities during the stage of progressive macrofailure (Fig. 7 III-IVb). Also, we noticed a growth and relaxation for tens of minutes in duration in the electrical parameter ΔU during the second and the third stages of deformation, reflecting an infiltration, a twinning processes and an evaporation of water within the cracks structures. Significant increases in ΔU have been recorded during the second stage of deformation macrofailures in all samples. This dynamics in ΔU did not correlate with variations in the applied stress and indicated the process of crack genesis and activation energy. The anomalies in electrical structure continued for dozens of minutes after a rock sample macrofailure testifying to a low velocity of relaxation processes. The main strain steps recorded during the fracture process of dry samples have not changed. However, the strength of moistened rocks decreased by 20 to 30% compared to that of same dry rocks. The decrease of strength of the moistened rock sample is caused by the increase of cracking rate and the adsorption phenomena. Signals of max AE amplitude arise and reach the maxima in the second stage of deformation. Figure 10 gives an example of acoustic signals recorded in granite sample in dry and moistened conditions. It is possible to conclude that AE activization appeared as result of pore collapse, and water diffusion inside the active cracks. The gradual migration of pore water to the microcracks field increased the stress around microdefects leading to an increase in the rate of cracking and their rapid development. The obtained AE behavior is similar

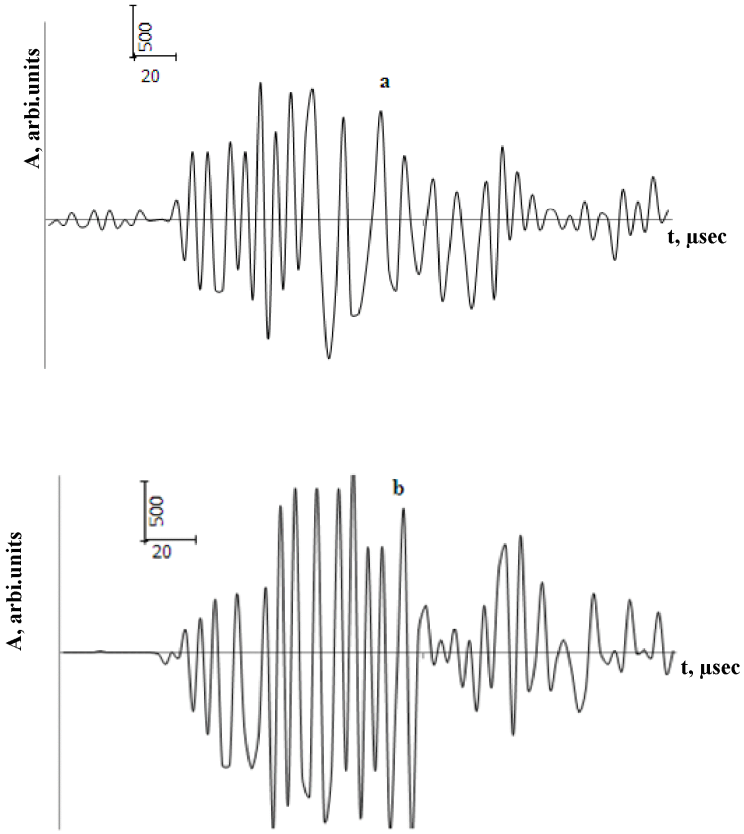

Fig. 10. AE signals recorded during the deformation of dry (a) and moistened (b) granite samples.

to the activity of earthquake swarms recorded in seismically active regions (Sobolev *et al*. 2010). In general, the moisture of crystalline rocks influenced the physical precursors of failure.

3.3.2 Influence of the deformation regime

Figure 7 I-Vc represents the experimental results during the variation of the deformation regime when the vertical load P was stabilized constant at stage (0.8 to 0.9)t_f and the horizontal load H decreased gradually until it became zero. We noted shrinkage in the third stage, C, of the deformation parameter $\mathcal{J}$, a strong increase of AE, an increase in AE during the second and third strain stages, an increase in V_P during the first stage of deformation and its decrease during the two last stages, non-noticeable variations of V_S. Electrical potential ΔU did not show a clear trend and its variation was generally

unremarkable, except for the pyrophyllite and concrete rock samples. As a result, a marked appearance of physical precursors in V_S and ΔU parameters was attenuated at this stage

3.3.3 Influence of uniaxial load and relatively high strain rate

Figure 7 I-Vd shows the experimental results when rocks samples were loaded under uniaxial stress at constant high strain rate ($10^{-6}s^{-1}$). A nearly linear trend of $\mathcal{J}$ parameter was recorded at the first strain stage, A, and its constancy at the second and third stages, B and C, exponential increase of AE during the stages, B and C, constancy in V_p during the second and the third stages of deformation, a decrease in V_S was recorded for the pyrophyllite during the third strain stage, ambiguous variations of V_S were unregistered for the rest of rocks and insignificant changes in ΔU compared to previous cases. It was difficult to identify the final stage of macrocracking by the parameters $\mathcal{J}$, V_P, and ΔU, however it was possible to identify the initial and the final stages of the failure by the AE. The measurements showed that duration of an EMR single pulse did not exceed 10 mcs.

3.3.4 Influence of temperature

The effect of temperature has an impact on the deformation of the rock. Results on temperature effect on the rock failure precursors were described in our previous work (Baddari *et al.* 2012). The brittle shear failure predominated at high temperatures. The $\mathcal{J}$ curve drifts leftward with the increase of temperature (Fig. 11 II-IIIa). This fact indicates that the increase of temperature led to an increase in the quantity of active cracks. The transition to the cracking phase was relatively fast at temperatures of 300-400 °C testifying to the brittle character of its rupture (Fig. 9 Ib, c). A shrinking of the maximum of the curve $\mathcal{J}$, with respect to the t/t_f-axis, was generally marked at high temperatures, for the rock samples, reflecting the weak occurrence of the quasi-plastic deformation of the sample. The V_P/V_S ratio at high temperatures (Fig. 11 II-IIIb) marked a significant decrease during the microfissuration stage. An extremum narrowing has been noted at 300 and 400 °C for all samples at the phase 0.4-05 t/t_f. The high temperature has increased the electrical parameters $\Delta\rho$ at 400 °C (Fig. 11 IIIc) and decreased ΔU at 300-400 °C (Fig. 11 II-IIId). However, at a temperature of 400 °C (Fig. 12), the amplitudes and periods of the EMR pulses have reached the maximum in the middle of the second stage of strain-stress rock state**,** which differs from the variation of these parameters under the conditions of room temperature. During the formation phase of isolated microcracks, the amplitude and the pulse period of EMR are much greater than those of AE. The

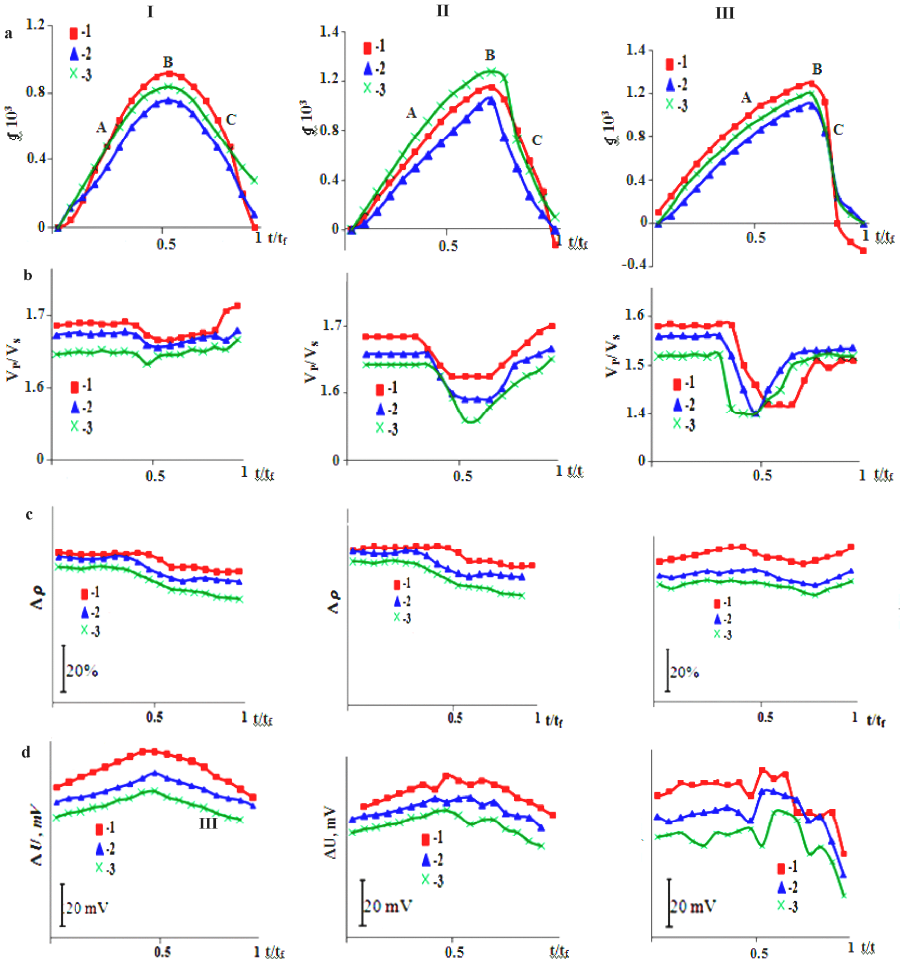

Fig. 11. Influence of temperatures on the physical precursors of the failure: first tensor invariant of flat deformation (a), V_P/V_S ratio (b), apparent electrical resistivity (c), and electrical potential (d). I-III – data obtained at T = 100-200, 300, and 400 °C respectively. 1 – granite, 2 – diabase, 3 – pyrophyllite.

synchronized recording of EMR and AE intensities showed that their variations have been influenced by applied temperature. At 400 °C EMR and AE events have been recorded practically at 0.3 [t/t_f] reflecting an early sample microfissuration (Fig. 13). In conclusion II curves of AE and EMR activities were drift rightward with increased temperatures. The gradual rise of load during the first phase of experiment was characterized by a low intensity of EMR and AE at 25 °C. The beginning of microcracking process clustering at

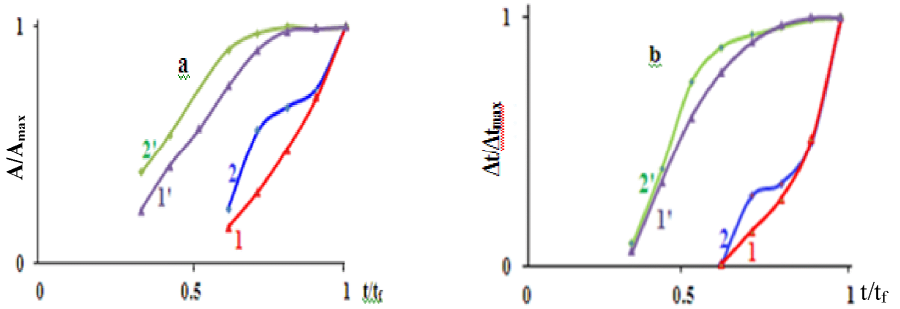

Fig. 12. Variations of the normalized amplitudes and the periods of AE (1) and EMR (2) at 25 °C and AE (1') and EMR (2') signals obtained at 400 °C for pyrophyllite sample.

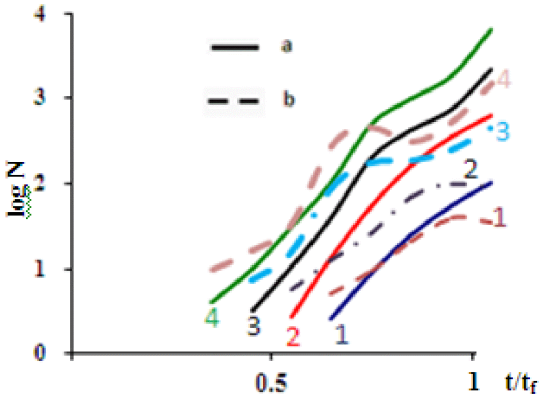

Fig. 13. The synchronized recording of AE (a) and EMR (b) intensities obtained at different temperatures. 1 – 25 °C, 2 – 100 °C; 3 – 300 °C, 4 – 400 °C for pyrophyllite sample.

t/t_f = 0.6-0.8 was characterized by a rise in EMR and AE intensities. Strong EMR signals were recorded in this phase reflecting the growth and relaxation dynamics of the stress distribution in the sample. Microscopic measurements and integrated recording of AE and EMR realized in the granite sample showed that small defects of 0.8-2.2 mm in size produced short acoustic signals (<500 μs duration), and longer EMR pulses (>1 ms), however shear fractures of 15-40 mm trigger longer AE pulses and short EMR ones. This result allows to conclude that large shear cracks seems have low EMR generating capacity. In general, the increase of the temperature of the deformed rock accelerated the microcracking accumulation and increased the EMR and AE intensities.

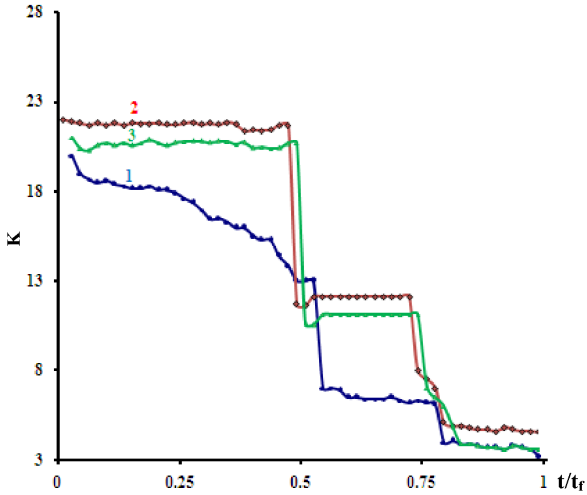

Fig. 14. Variations of parameter K at various temperatures for the dry diabase sample at 25 °C (1), 400 °C (2), and moistened sample (3).

3.4 The coalescence criterion

The coalescence criterion K kept a relative same morphology under various strain conditions as it has been obtained in Baddari *et al.* (2012). For the dry sample loaded at room temperature, the decrease of K appears much slower than in the case of moistened rocks and high temperature. The moisture and the increase in temperature generated a slip in the variations stages of K and an early transition to the irreversible deformation stage (Fig. 14, curves 2-3) which has been expanded with increasing temperature. The macrofracturing phase The macofracturing phase became faster and shorter at 0.5 [t/t_f]. We obtained practically the same variation form of K for all rock samples.

3.5 Statistical analysis of the joint physical field measurements

For convolution, several physical parameters were processed using natural orthogonal functions. In keeping with Baddari *et al.* (1999), and Sobolev (1995), the complex parameter was calculated by

$$S_k = \sum U_{ij} \varphi_{ik} \ , \tag{14}$$

where U_{ij} are the normalized values of the i-th physical parameter in the j-th point of measuring stress P, φ_{ik} are the eigenvectors of the correlation matrix of the measured physical parameters. Equation 15 is a result of convolution of a set of k physical parameters through a complex parameter S_k. Details on the chosen statistical method are explained in Baddari *et al.* (1999). Equa-

tion 14 is a result of convolution of a set of physical parameters through a complex parameter S_k.

To find out regularities in variation of complex parameters S_k, the measurements data for each of the tested samples were split into two groups. The first included points and routes measured in macrofailure areas, the second – those of the areas with no registered macrocracks. Accordingly, correlation matrixes for each group were compiled, reflecting changes in different physical parameters, and generalized values of eigenvectors were found. Six physical parameters have been considered: facet plane strain tensor ($\mathcal{J}$), longitudinal elastic wave velocity (V_P), EMR and AE intensities (N_{EMR} and N_{AE}), electrical resistivity and electrical potential changes ($\Delta\rho$ and ΔU). Computation of correlation matrixes showed that certain parameters are closely correlated regardless of the type of a sample tested. The correlation matrixes reveal invariably high correlation coefficients between the acoustic parameters N and V_P, on the one hand, and electrical $\Delta\rho_a$ and ΔU – on the other, no matter what the material. The study of six complex parameters S_k (k = 1,…, 6) computed by formula 14 with concrete values of eigenvectors φ_{ik} taken into account showed that bulk of information (95-98%) comes from the first two complex parameters – S_1 and S_2, while the equations for both parameters for the areas that were or were not brought to macrofailure differ greatly.

Despite a considerable dissimilarity in mechanical properties of samples, the complex parameters S_2 prove morphologically identical. Parameter S_2 is bay-shaped in form, which makes it more promising in terms of prognosis. Figure 15 gives changes in the complex parameter S_2 for portions brought to

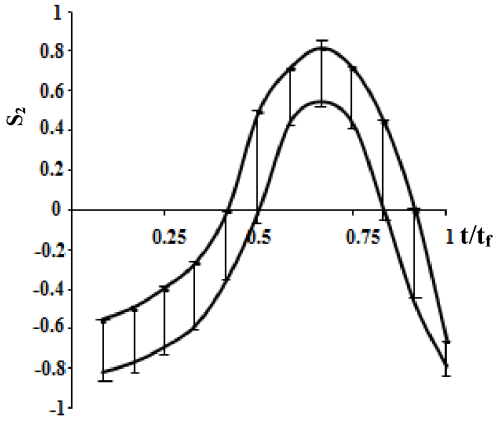

Fig. 15. Variations of the complex parameter S_2 illustrating the succession of the formation of the macrofailure in the rock sample. Same shaded is the area of variation of S2 for the studied rock samples and stress-strain conditions.

failure at different experimented strain conditions. The analysis of the complex parameter S_2 behaviour in macrofailure zone enabled to point out the following dependence of the S_2 value and its curve on strain and failure. Negative values of S_2 in the initial stage of the graph are characteristic of quasi-elastic deformations. The second stage in its behaviour is marked by a gradual rise in positive values up to maximal, which corresponded to microcracks concentration up to critical. The third, and the final stage, which manifests itself in a sharp fall of S_2 following the maximum, testifies to the process of large cracks formation along with a rise in unstable deformation in the failing portions of the samples. Identification of this stage by graph S_2 may serve as a macrofailure precursor. These three characteristics are valid for all the studied rock types. The analysis of S_2 morphology for the series of four tests showed good stability of this parameter (Fig. 15). Thus, the conditions of rock deformation affected individual physical precursors and did not qualitatively change the evolution of rock micro and macrofailure.

4. DISCUSSION OF RESULTS AND CONCLUSIONS

The use of large rock samples in our tests permits simulation of the fracturing process and utilization of a dense network for observation of the space – time variation of several physical fields. The experiments show that the reproducibility of measurements depends on the high resolution of the used laboratory equipment, the methods of measurements and the distribution of measurement network on different areas of rock sample. The errors of the acquired data for different physical fields are acceptable. The experiments were performed on solid rock samples with artificial defects acting as stress concentrators, which allowed simulation of internal shear failure. Each rock sample is characterized by a specific crystalline textural structure, with some strength distribution of grain contacts, grain interiors and intergrain zones. The process of deformation and failure of such a structure under load are accompanied by changes of these distributions caused by destruction of bonds as the weakest contacts and formation of microfailures.

After experiments using dry samples, a structural discreetness of the rock sample has been obtained. The tested rocks were divided into separate blocks by echelons of cracks of different size and orientations. Statistical processing of the geometric average sizes showed the ratio of the neighboring failures average sizes L_i/L_{i-1} is close to 2.7-3. In accordance with Sadovsky *et al*. (1991) and Sobolev (1995), the average ratio of adjacent basic dimensions of the seismogenic blocks after a seismic main shock in the geophysical environment is $L_i/L_{i-1} = 3.33$, which testifies to the self-similarity of the seismic process at different scales, and consequently the idea that structural discreetness of the earth and its discontinuity are one and the same thing. It should be noted that faultings in the earth crust after an earthquake

are also accompanied by volume units and widths of the faults may reach tens or hundreds of meters (Kuksenko *et al*. 2009).

The transition from a low level to a higher one occurs when the crucial concentration of cracks of appropriate dimensions is attained in the failure focus. This concentration depends on the sizes of forming cracks. The transition from micro to macrocracks in loaded object takes place upon reaching a certain crucial concentration of cracks of appropriate dimensions in the failure source. The critical factor, here, is the crack concentration parameter K (Baddari *et al.* 1996, Zavyalov 2006). This parameter characterizes the cracks mutual interaction of and their ability to merge via local stress field. $K = 3.8$ constitutes the threshold of the migration of the rock to the progressive macrocrack process.

The failure development process in dry samples follows three main stages: nonuniform and isolated spatial distribution of microcracks, nucleation of macrofailure source, propagation and expansion of the macrofailure. Non homogeneous distribution of the rock spatial crystalline structure subject to load leads to a mosaic distribution of EMR and AE characteristics. As a result, the crack scale effect has been observed in the EMR and AE structure behaviors. At the formation phase of isolated microcracks, the amplitude and the pulse period of EMR are much greater than those of AE. The transition of the material to the third phase of deformation (the progressive macro failure) triggers off a reverse relationship: the pulse quantity, as well as the amplitudes and periods, increases highly. The most important emissions activities have been recorded in the influence zone of the stress concentrators, where the main crack has been localized at the end of the experiment. An inequality in the intensities of AE and EMR has been noted. We note that EMR is more sensitive to the generation of tensile cracks than shear ones. Acoustic and electromagnetic quiescences have been recorded during different phases of sample deformation. This phenomenon has been recorded during different phases of rock deformation. The recorded quiescence is probably related to the scenario preceding various cracking levels transitions and consequently an avalanche in the course of expanding failure.

The evolution of the crack is controlled by the stability and interaction of ruptures in the stress strain field. This transformation is a result of reorganization in the rock of ionic and electronic physical subsystems, which must lead to characteristic changes of the mechanical and electrical properties depending on the strain-stress state of rock. The experimental results testify to important fluctuations in mechanical, and electrical parameters recorded in rock samples under various strain conditions. These fluctuations have certain common characteristics such as the transition through extremums and a developed dispersion in physical precursors during the prefailure stage. Observation and analysis of all the precursors enabled us to forecast the time of

main failure to within 60-20 min. The last precursors to be recorded were observed a few minutes before the final macrofailure in strain and electrical parameters. Basing on the character of changes of physical precursors, the rock has been divided in the zones of increased and decreased danger of the brittle failure, *i.e.*, into separate blocks, according to echelons of cracks of different sizes and directions. The analysis of the velocity variations showed, in some experiments, that if a zone is characterized by a low velocity, then a domain of high velocity will be formed around it and *vice versa*. It was found that above about one half of the failure strength the average velocity became a non-linear function of the load. In all samples, the velocity V_P reached maximum values at 0.4-0.5 [t/t_f], possibly due to the developing fracture nucleus (Fig. 7 IIIa). This maximum in V_P has been observed shortly before for the other samples. Increases in V_P have been recorded just before the main failure formation in the end of experiments. V_S marked practically the same trend as V_p but weaker (Fig. 7 IVa). Maximum values for V_S have been noted for the pyrophyllite and concrete samples at 0.4-0.5 [t/t_f]. Immediately after, V_S increased and decreased till 0.9 [t/t_f], reflecting a beginning of accumulation of shear damages at this stage. Strong increases in V_S have been recorded prior to macrofailure of diabase, pyrophyllite and concrete samples, which testifies to the heterogeneous field of strains resulting by the main failure expansion and the medium division into areas of unstable and elastic deformation. Anisotropies have been recorded in velocities in the directions x and y, parallel and perpendicular respectively to the direction of the main load P (Fig. 8). A considerable degree of elastic anisotropy is developed prior to failure. This is due to oriented microcracks, which play a major role in the failure process itself. The observed velocity anisotropy was found to be associated with changes in micro cracks density and distribution pattern. We noticed an increase in anisotropy prior to the macro failure. The maximum of this increase coincided with the dynamic propagation of the macrofailure structure. Local variations of apparent resistivity $\Delta\rho_a$ were detected. In certain zones, resistivity anisotropy was found to develop over time (Fig. 9). The anisotropy detected at the initial stage of loading is associated with the failure of the preexisting defects. As the stress increases, the portion of progressively smaller defects among the failed defects increases. The anisotropy can be qualitatively explained by the development of oriented cracks. The decrease of $\Delta\rho_a$ could be due to expansion of conducting paths system in room humidity (40-60%) experiment and crack accumulation within rock sample. The increase in $\Delta\rho_a$ is probably caused by coalescing failures, the rupture of the channels of current conduction and the formation of the macrofailure (Baddari *et al.* 1999, Ponomarev 1987, Sobolev 1995, Stopiński *et al.* 1991). It can be concluded that the variation of $\Delta\rho_a$ in the area of incipient macrofailure are upper in value and often of

the opposite polarity compared with the stable areas variations. The variations of $\Delta\rho_a$ depend on the surface of the studied area and localization of the measurement sensors in relation to the mechanical stress concentration, the orientations of cracks and the path of the macrofailure propagation. We can deduce that stressed rocks prior to macrofailure at different scales should be characterized by a heterogeneous field of strains. Polarity in $\Delta\rho_a$ changes registered in different positions, with regard to incipient failure zones, may be explained by the heterogeneities of the rock structure and the rock medium division into areas of unstable and elastic deformation. Laboratory and *in situ* investigations revealed that separate active strain regions are formed prior the macrofailure (Baddari and Frolov 2010, Sobolev 1995, Stopiński *et al.* 1991).

As the sample was loaded, the spontaneous electric field ΔU changed significantly (Fig. 7Va). We have recorded some cases of initiation and disintegration of local electric anomalies when the load varied in the range of time (0.5-0.9) t/t_f. Increases in ΔU have been recorded in all cases except in the pyrophyllite sample just before the end of the experiment. Some anomalies reached a maximum of about 30 mV at the beginning of final failure stage. Its lifetime has changed from 20 to 50 min, the reason being probably attributed to electric relaxation phenomenon. When the ΔU remained constant, we did not observe failures occurring at a higher scale. The fast transition of the failure to high scale, which led to the formation of the macrofailures and the redistribution of the stress in the rock sample, corresponded to important variation of the electric field. A nonlinear relation between the mechanical and electric fields after loading, the variations of the surface electric field significantly decreased. A number of features observed in the electric disturbances seem to be explainable qualitatively within the framework of ionic migration mechanisms.

The variations in elastic wave velocities and the electric parameters must, to a certain extent, mirror the strain-stress state of a rock and the development of anisotropy in it. The anisotropy of strength and the distributions of mechanical stresses in deformed rock massif are often a reason of local dominance of brittle destruction, resulting in catastrophical phenomena (earthquakes, rockbursts, collapses, *etc*.).

The features of the failure process refer to various conditions of rock mechanical loading. It was obtained that the negative feedback of loading of rock samples enabled to prolong the macrofailure growth stage and to study in details some regularities in main crack evolution. The macrofailure growth observed in these experiments was studied in our previous work (Baddari and Frolov 2010). It was established that moisture was accompanied by increasing the number of microcracks sets, and consequently intense AE and EMR activities in deformed rocks. The detailed observation of phys-

ical precursor variations shows that moisture increases the strain rate. The fast drop of the parameter K at 0.5 [t/t_f] (Fig. 14) testifies that the fracturing begins and develops more intensively in the rock sample under the actions of the loading and moisture. Before loading, water fills all defects (pores, capillaries, pre-existed cracks) in the rock material. Under the action of external load, during the second stage of deformation, when fracture nucleuses arise and begin to grow, the intergranular space increases causing, the diffusion of water in the rock body. We can admit that the velocity of water diffusion can be higher that the dilatancy one. The water fills the opening cracks, causes much stresses on their surfaces, induces an electrokinetic effect, affects their mechanical features, develops more cracks clusters, and causes the formation of new damages in the sample. The molecules of water play, moreover, appreciably hydrolytic role in the fracture of the interatomic bonds and changes in the physical properties in the rock material. It can be assumed that the water may have a crucial effect, rather than crack genesis and activation energy. The early transition to irreversible deformation stage and the expansion of the latter has been recorded in the first flat deformation tensor $\mathcal{J}$ and the crack concentration parameter K in the case of the moistened rocks. The moisture content of 0.3-5%, depending on nature of each rock, significantly increases the second phase (stage B of $\mathcal{J}$) of deformation with any constant deformation rate. At a lower stress level, the wet rock has a plastic deformation higher than that for a dry sample. The pore pressure can be approximately described by Terzaghi's law (Terzaghi 1925). The fluid pressure has not been controlled, and consequently the effective pressure ($P_{\text{eff}} = P - P_{\text{H2O}}$) has not been measured in our tests. According to Althaus *et al.* (1994), the resulting pressure differences can easily reach values of some hundreds of MPa and locally exceed by far the applied confining pressure. We admit that effective pressure calculated by the Terzaghi's law increases the crack rate. We admit that pore fluid pressure shift the Mohr-circle to the left and closer to the Mohr–Coulomb failure envelop. The second stage of moistened rock deformation led to decreases in wave velocities, and increases followed by decreases in the electric potential. It should be noted that there is a relative increases of ΔU at the last phase of the second strain stage for the granite and the pyrophyllite samples. When the effect of moisture has been weakened as a result of its large dispersion over the sample body, its evaporation and reduction the potential energy in the end of this stage, the rock passed to a fast unstable and progressive macrofailure at the last deformation stage.At this stage the elastic wave velocities and the electric potential tend to decrease. As a result, the water saturation plays active role in lowering the strength of the rock sample, decreases its elastic limit, Young's modulus, affects its internal structure, and we obtain finally large damage accumulation

in the condition of lower loading compared with the case of dry rocks. Similar idea is claimed by Kuksenko *et al*. (2011).

During variation of the deformation regime (Fig. 5 I-Vc), we noted shrinkage in stage *C* of the rock. We can deduce that the prediction of dynamic failure on recorded variations of physical parameters cannot always be universal. It depends on loading regime, the nature of the used sample, and its degree of anisotropy.

In case of different strain rates, it should be noted that there is a relation between the final stage of macrofailure focus development and the strain rate of a loaded rock. The stepwise failure localization did not occur during the rock deformation with a fast strain rate ($10^{-6}s^{-1}$). In studied deformed rocks, the failure growth depended on the growth rate, as the growth rate is low. It was not possible to forecast in details the onset of macrofailure and to determine the instant of time at which the transition from the first stage to the second begins. Therefore, it should be said that the precursors time prediction is inversely proportional to the strain rate. Under conditions prevailing in some seismoactive regions, the rate of the strain is in order of $10^{-14}s^{-1}$ (Baddari *et al.* 1999, Sobolev 1995). The uncertainly in forecasting the time, extrapolated from our laboratory results to the earth scale, may be in the order of few months to a few years.

The rise in temperature from 25 up to 400 °C showed a variation of physical precursors of failure, especially at the intermediate and final stages of the rock failure. The high temperature showed a noticeable effect on the period and amplitude of the impulses (Fig. 12), as well as on the intensity of the acoustic and especially electromagnetic emissions (Fig. 13), which reflected changes in the corresponding microcracking process. This was manifested in the fast decrease of the parameter *K* (Fig. 14), which is probably due to the decrease in the plasticity of the grains and the transition to a more brittle rupture of the inter-grains contacts as a result of gravitational evaporation of the rock moisture and explosion of liquid or gaseous inclusions and microfracture (Baddari and Frolov 1990, Corrêa and Nascimento 2005, Lavrov and Shkuratnik 2005, Panin 1985). The applied temperatures in these experiments are different from the temperatures of recrystallization and other second-type transition phases in the studied rocks. The variation of physical precursors is certainly related to the quantity and changes of the state of adsorbed fluids in the pores of polycrystalline field. In general, an increase of temperature has led to the predominance of the brittle fracture mechanism, which led to reduction of the plastic limit and its extension in time following the formation of spatially separate cracks. In our opinion, high applied temperatures were accompanied by an increase of the proportion of intercrystalline failure and brittle crystal boundaries microcracks. For well-studied brittle materials it was noted that subcritical crack propagation rate

was determined by the rate of chemical reaction at the crack tip (Beeler 2004, Atkinson and Meredith 1987). The final stage of macrofailure genesis rupture was accelerated while the temperatures became significant.

The analysis of a set of physical fields makes the precursor identification more unambiguous and practically dependable. The obtained results testify to the considerable fluctuations in strain, acoustic, electromagnetic, and electrical parameters recorded in natural rocks and concrete material under various strain conditions. Based on these experiments, the form of these fluctuations differs not only for physically different fields, the nonhomogeneity of the stress-strain distribution and the anisotropy of the rock medium but also for realizations of an individual parameter registered in different frequency ranges, bases, and orientations. The differences in the time changes of the physical precursors caused by micro and macrofailure allow to assume that all investigated parameters are not equivalent. Various strain conditions change the tendency of each physical parameter. The complex statistical analysis obtained after convolution of measurement results allowed to reliably forecast the different failure stages independently of the composition, nature, and experimental conditions. The increase of S_2 to a maximum, followed by a sharp decrease can be used as a predictor of macrofailure in particular parts of the rock mass. The result provided in Fig. 15 makes S_2 more promising in terms of prognosis. The strain, the acoustic, the coalescing and the complex parameters appear to be useful in using them as physical precursors of fracture in arid, geothermal, and vadoze zones. The wave velocities, the electrical, the coalescing and the complex parameters can be used in order to investigate the fracture precursors in geothermal region. The obtained results point out the efficiency of laboratory modelling of seismic process in the earth crust.

Acknowledgments. The authors would like to express their gratitude to Dr. Mathilde Adelinet and to the two anonymous referees for their helpful criticism, fruitful and valuable comments.

References

Adushkin, V.V., and S.B. Turuntaev (2005), Anthropogenic processes in the earth's crust. **In:** *Risks and Catastrophes*, INEK, Moscow.

Althaus, E., A. Friz-Töpfer, Ch. Lempp, and O. Natau (1994), Effects of water on strength and failure mode of coarse-grained granites at 300 °C, *Rock Mech. Rock Eng.* **27**, 1, 1-21, DOI: 10.1007/BF01025953.

Ammon, Ch.J., H. Kanamori, and Th. Lay (2008), A great earthquake doublet and seismic stress transfer cycle in the central Kuril islands, *Nature* **451**, 561-565, DOI: 10.1038/nature06521.

Asatryan, Kh.O., G.A. Sobolev, and V.A Mansurov (1993), Development of block hierarchy and acoustic emission in rock at all-sided compression. **In**: *Modeling of the Seismic Process and Earthquake Precursors*, Vol. 1, RAS, 17-20 (in Russian).

Atkinson, B.K., and P.G. Meridith (1987), Experimental fracture mechanics data for rocks and minerals. **In:** B.K. Atkinson (ed.), *Fracture Mechanics of Rock,* Academic Press, San Diego, CA, 477-525.

Baddari, K., and A.D. Frolov (1990), Influence of temperature on physical precursors of rock failure, *Izv. Geol. Prospect.* **9**, 102-108 (in Russian).

Baddari, K., and A.D. Frolov (2010), Regularities in discrete hierarchy seismo-acoustic mode in a geophysical field, *Ann. Geophys.-Italy* **53**, 5-6, 31-42, DOI: 10.4401/ag.4725.

Baddari, K., G.A. Sobolev, and A.D. Frolov (1996), Similarity in seismic precursors at different scales, *CR Acad. Sci. II A* **323**, 755-763.

Baddari, K., G.A. Sobolev, A.D. Frolov, and A.V. Ponomarev (1999), An integrated study of physical precursors of failure in relation to earthquake prediction, using large scale rock blocks, *Ann. Geophys.-Italy* **42**, 5, 771-787.

Baddari, K., A.D. Frolov, V. Tourtchine, and F. Rahmoune (2011), An integrated study of the dynamics of electromagnetic and acoustic regimes during failure of complex macrosystems using rock blocks, *Rock Mech. Rock Eng.* **44**, 3, 269-280, DOI: 10.1007/s00603-010-0130-5.

Baddari, K., A.D. Frolov, V. Tourtchine, S. Makdeche, and F. Rahmoune (2012), Effect of temperature on physical precursors of block rock failure, *Acta Geophys*. **60**, 4, 1007-1029, DOI: 10.2478/s11600-012-0038-4.

Bahat, D., A. Rabinovitch, and V. Frid (2005), *Tensile Fracturing in Rocks: Tectonofractographic and Electromagnetic Radiation Methods*, Springer Verlag, Berlin.

Beeler, N.M. (2004), Review of the physical basis of laboratory-derived relations for brittle failure and their implications for earthquake occurrence and earthquake nucleation, *Pure Appl. Geophys.* **161**, 9-10, 1853-1876, DOI: 10.1007/s00024-004-2536-z.

Benson, P.M., B.D. Thompson, P.G. Meredith, S. Vinciguerra, and R.P. Young (2007), Imaging slow failure in triaxially deformed Etna basalt using 3D acoustic-emission location and X-ray computed tomography, *Geophys. Res. Lett.* **34**, 3, DOI: 10.1029/2006GL028721.

Bizzarri, A., and M. Cocco (2006), A thermal pressurization model for spontaneous dynamic rupture propagation on a three-dimensional fault: 2. Traction evolution and dynamic parameters, *J. Geophys. Res.* **111**, B05304, DOI: 10.1029/2005JB003864.

Brace, W.F., and D.L. Kohlstedt (1980), Limits on lithospheric stress imposed by laboratory experiments, *J. Geophys. Res.* **85**, B11, 6248-6552, DOI: 10.1029/JB085iB11p06248.

Cai, M., and D. Liu (2009), Study of failure mechanism of rock under compressive-shear loading using real-time laser holography, *Int. J. Rock Mech. Min.* **46**, 1, 59-68, DOI: 10.1016/j.ijrmms.2008.03.010.

Chen, F., D.Y. Chen, Q.-P. Cao, S.-J. Yu, D.-J. Xu, C.-X. Chen, Y.-L. Yu, and J.-H. Sheng (1993), Study on the property of apparent resistivity changes of rock samples by in situ shear and friction test, *Acta Seismol. Sinica* **6**, 3, 721-279, DOI: 10.1007/BF02650411.

Corrêa, C.C., and R.S.V. Nascimento (2005), Study of shale-fluid interactions using thermogravimetry, *J. Therm. Anal. Calorim.* **79**, 2, 295-298, DOI: 10.1007/s10973-005-0052-8.

Darot, M., and T. Reuschlé (2000), Acoustic wave velocity and permeability evolution during pressure cycles on a thermally cracked granite, *Int. J. Rock Mech. Min.* **37**, 7, 1019-1026, DOI: 10.1016/S1365-1609(00)00034-4.

David, C., B. Menéndez, and M. Darot (1999), Influence of stress-induced and thermal cracking on physical properties and microstructure of La Peyratte granite, *Int. J. Rock Mech. Min.* **36**, 4, 433-448, DOI: 10.1016/S0148-9062(99)00010-8.

Dresen, G., S. Stanchits, and E. Rybacki (2010), Borehole breakout evolution through acoustic emission location analysis, *Int. J. Rock Mech. Min.* **47**, 3, 426-435, DOI: 10.1016/j.ijrmms.2009.12.010.

Evans, K.F. (2005), Permeability creation and damage due to massive fluid injections into granite at 3.5 km at Soultz: 2. Critical stress and fracture strength, *J. Geophys. Res*. **110**, B4, DOI: 10.1029/2004JB003169.

Fortin, J., S. Stanchits, S. Vinciguerra, and Y. Guéguen (2011), Influence of thermal and mechanical cracks on permeability and elastic wave velocities in a basalt from Mt. Etna volcano subjected to elevated pressure, *Tectonophysics* **503**, 60-74, DOI: 10.1016/j.tecto.2010.09.028.

Frid, V., A. Rabinovitch, and D. Bahat (2003), Fracture induced electromagnetic radiation, *J. Phys. D. Appl. Phys*. **36**, 13, 1620-1628, DOI: 10.1088/0022-3727/36/13/330.

Glover, P.W.J., J.B. Gomez, P.G. Meredith, S.A. Boon, P.R. Sammonds, and S.A.F. Murrell (1996), Modelling the stress-strain behaviour of saturated rocks undergoing triaxial deformation using complex electrical conductivity measurements, *Surv. Geophys.* **17**, 3, 307-330, DOI: 10.1007/BF01904046.

Gupta, H.K. (2005), Artificial water reservoir-triggered earthquake with special emphasis at Koyna, *Curr. Sci. India* **88**, 10, 1628-1631.

Heap, M.G., S. Vinciguerra, and P.G. Meredith (2009), The evolution of elastic moduli with increasing crack damage during cyclic- stressing of basalt from Mt. Etna volcano, *Tectonophysics* **471**, 1-2, 153-160, DOI: 10.1016/j.tecto.2008.10.004.

Heap, M.J., P. Baud, P.G. Meredith, S. Vinciguerra, A.F. Bell, and I.G. Main (2011), Brittle creep in basalt and its application to time-dependent volcano deformation, *Earth Planet. Sci. Lett.* **307**, 1-2, 71-82, DOI: 10.1016/j.epsl.2011.04.035.

Jouniaux, L., K. Masuda, X. Lei, O. Nishizawa, K. Kusunose, L. Liu, and W. Ma (2001), Comparison of the microfracture localization in granite between fracturation and slip of a preexisting macroscopic healed joint by acoustic emission measurements, *J. Geophys. Res.* **106**, B5, 8687-8698, DOI: 10.1029/2000JB900411.

Jouniaux, L., M. Zamora, and T. Reuschlé (2006), Electrical conductivity evolution of non-saturated carbonate rocks during deformation up to failure, *Geophys. J. Int.* **167**, 2, 1017-1026, DOI: 10.1111/j.1365-246X.2006.03136.x.

Kadomtsev, A.G., E.E. Damaskinskaya, and V.S. Kuksenko (2011), Fracture features of granite under various deformation conditions, *Phys Solid State* **53**, 9, 1876-1881, DOI: 10.1134/S1063783411090150.

Kuksenko, V.S. (2005), Diagnostic and forecasting of breakage of large-scale objects, *Phys. Solid State* **45**, 5, 812-816, DOI: 10.1134/1.1924837.

Kuksenko,V.S., Kh.F. Makhmudov, V.A. Mansurov, U. Sultonov, and M.Z. Rustamova (2009), Changes in structure of natural heterogeneous materials under deformation, *J. Min. Sci.* **45**, 4, 355-358, DOI: 10.1007/s10913-009-0044-3.

Kuksenko, V.S., E.E. Damaskinskaya, and G. Kadomtsev (2011), Fracture of granite under various strain conditions, *Izv. Phys. Solid Earth* **47**, 10, 879-885, DOI: 10.1134/S1069351311100053.

Lacidogna, G., A. Carpinteri, A. Manuello, G. Durin, A. Schiavi, G. Niccolini, and A. Agosto (2011), Acoustic and electromagnetic emissions as precursor phenomena in failure processes, *Strain* **47**, Suppl. s2, 144-152, DOI: 10.1111/j.1475-1305.2010.00750.x.

Lavrov, A.V., and V.L. Shkuratnik (2005), Deformation- and fracture-induced acoustic emission in rocks, *Acoust. Phys.* **51**, Suppl. 1, 2-11, DOI: 10.1134/1.2133948.

Lockner, D. (1993), The role of acoustic emission in the study of rock, *Int. J. Rock Mech. Min.* **30**, 7, 883-899, DOI: 10.1016/0148-9062(93)90041-B.

Lockner, D.A., and J.D. Byerlee (1986), Changes in complex resistivity during creep in granite, *Pure Appl. Geophys.* **124**, 4-5, 659-676, DOI: 10.1007/BF00879603.

Lockner, D.A., and S.A. Stanchits (2002), Undrained poroelastic response of sandstones to deviatoric stress change, *J. Geophys. Res.* **107**, B12, 2553, DOI: 10.1029/2001JB001460.

Lockner, D.A., J.D. Byerlee, V.S. Kuksenko, and A.V. Ponomarev (1986), Stick slip, charge separation and decay, *Pure Appl. Geophys.* **124**, 3, 601-608, DOI: 10.1007/BF00877218.

Lockner, D.A., J.D. Byerlee, V.S. Kuksenko, A. Ponomarev, and A. Sidorin (1991), Quasi-static fault growth and shear fracture energy in granite, *Nature* **350**, 6313, 39-42, DOI: 10.1038/350039a0.

Panin, V.E. (1985), *Structural Levels of Solid Bodies' Deformation*, Nauka, Novosibirsk (in Russian).

Ponomarev, A.V. (1987), The study of variations in the electrical state of rocks as applied to the search for earthquake precursors, Ph.D. Thesis, Moscow (in Russian).

Ponomarev, A.V., A.D. Zavyalov, V.B. Smirnov, and D.A. Lockner (1997), Physical modelling of the formation and evolution of seismically active fault zones, *Tecnophysics* **277**, 57-81, DOI: 10.1016/S0040-1951(97)00078-4.

Pozzi, J.-P., and L. Jouniaux (1994), Electrical effects of fluid circulation in sediments and seismic prediction, *CR Acad. Sci. II A* **318**, 1, 73-77.

Reuschlé, T., S.G. Haore, and M. Darot (2006), The effect of heating on the microstructural evolution of La Peyratte granite deduced from acoustic velocity measurements, *Earth Planet. Sci. Lett*. **243**, 3-4, 692-700, DOI: 10.1016/j.epsl.2006.01.038.

Rudajev, V., J. Vilhelm, J. Kozák, and T. Lokajíček (1996), Statistical precursors of instability of loading rock samples based on acoustic emission, *Int. J. Rock Mech. Min.* **33**, 7, 743-748, DOI: 10.1016/0148-9062(96)00023-X.

Sadovsky, M.A., L.G. Bolkhovitinov, and V.F. Pisarenko (1991), *Deformation of the Geophysical Medium and Seismic Process*, Nauka, Moscow (in Russian).

Schubnel, A., and Y. Guéguen (2003), Dispersion and anisotropy of elastic waves in cracked rocks, *J. Geophys. Res*. **108**, B2, 1978-2012, DOI: 10.1029/2002JB001824.

Schubnel, A., B.D. Thompson, J. Fortin, Y. Guéguen, and R.P. Young (2007), Fluid induced rupture experiment on Fontainebleau sandstone: Premonitory activity, rupture propagation, and aftershocks, *Geophys. Res. Lett.* **34**, 19, DOI: 10.1029/2007GL031076.

Shearer, P.M. (1999), *Introduction to Seismology*, Cambridge Univ. Press, Cambridge.

Simpson, D.W., W.S. Leith, and C.H. Sholz (1988), Two types of reservoir- induced seismicity, *Bull. Seismol. Soc. Am.* **78**, 6, 2025-2040.

Smirnov, V.B., and A.V. Ponomarev (2004), Seismic regime relaxation properties from in situ and laboratory data, *Izv. Phys. Solid Earth* **40**, 10, 807-816.

Smirnov, V.B., A.V. Ponomarev, and A.D. Zavyalov (1995), Acoustic structure in rock samples and the seismic process, *Izv. Phys. Solid Earth* **31**, 1, 38-58.

Smirnov, V.B., A.V. Ponomarev, P. Bernard, and A.V. Patonin (2010), Regularities in transient modes in the seismic process according to the laboratory and natural modelling, *Izv. Phys. Solid Earth* **46**, 2, 104-135, DOI: 10.1134/S1069351310020023.

Sobolev, G.A. (1995), *Fundamental of Earthquake Prediction*, ERC, Moscow.

Sobolev G.A., and A.V. Ponomarev (2003), *Physics of Earthquakes and Precursors*, Nauka, Moscow (in Russian).

Sobolev, G.A., and A.V. Ponomarev (2011), Dynamics of fluid-triggered fracturing in the modeles of a geological medium, *Izv. Phys. Solid Earth* **47**, 10, 902-918, DOI: 10.1134/S1069351311100119.

Sobolev, G.A., A.V Ponomarev, Yu.Ya. Maibuk, N.A. Zakrzhevskaya, V.I. Ponyatovskaya, D.G. Sobolev, A.A. Khromov, and Yu.V. Tsyvinskaya (2010), The dynamics of the acoustic emission with water initiation, *Izv. Phys. Solid Earth* **46**, 2, 136-153, DOI: 10.1134/S1069351310020035.

Soloviev, S.P., and A.A. Spivak (2009), Electromagnetic signals generated by the electric polarization during the constrained deformation of rocks, *Izv. Phys. Solid Earth* **45**, 4, 347-355, DOI: 10.1134/S1069351309040077.

Stanchits, S.A., D.A. Lockner, and A.V. Ponomarev (2003), Anisotropic changes in P wave velocity and attenuation during deformation and fluid infiltration of granite, *Bull. Seismol. Soc. Am.* **93**, 4, 1803-1822, DOI: 10.1785/0120020101.

Stopiński, W., A.V. Ponomaryov, and V. Los (1991), The dynamics of rupture in porous media, *Pure Appl. Geophys*. **136**, 1, 29-47, DOI: 10.1007/BF00878886.

Terzaghi, K. (1925), *Principles of Soil Mechanics: A Summary of Experimental Studies of Clay and Sand*, McGraw-Hill, New York.

Thompson, B.D., R.P. Young, and D.A. Lockner (2006), Fracture in Westerly granite under AE feedback and constant strain rate loading: Nucleation, quasi-static propagation, and the transition to unstable fracture propagation, *Pure Appl. Geophys*. **163**, 5-6, 995-1019, DOI: 10.1007/s00024-006-0054-x.

Vinciguerra, S., C. Trovato, P.G. Meredith, and P.M. Benson (2005), Relating seismic velocities, thermal cracking and permeability in Mt. Etna and Iceland basalts, *Int. J. Rock Mech. Min.* **42**, 7-8, 900-910, DOI: 10.1016/j.ijrmms.2005.05.022.

Wan, Z.J., Y.S. Zhao, Y. Zhang, and C. Wang (2009), Research status quo and prospection of mechanical characteristics of rock under high temperature and high pressure, *Procedia Earth Planet. Sci*. **1**, 1, 565-570, DOI: 10.1016/j.proeps.2009.09.090.

Xu, X.L., F. Gao, X.M. Shen, and H.P. Xie (2008), Mechanical characteristics and microcosmic mechanisms of granite under temperature loads, *J. China Univ. Min. Technol*. **18**, 3, 413-417.

Zang, A., F.C. Wagner, S. Stanchits, Ch. Janssen, and G. Dresen (2000), Fracture process zone in granite, *J. Geophys. Res*. **105**, B10, 23651-23661, DOI: 10.1029/2000JB900239.

Zavyalov, A.D. (2006), *Intermediate Term Earthquake Prediction*, Nauka, Moscow.

Zhang, L.Y., X.B. Mao, and A.H. Lu (2009), Experimental study of the mechanical properties of rocks at high temperature, *Sci. China Ser. E* **52**, 3, 641-646, DOI: 10.1007/s11431-009-0063-y.

Zhurkov, S.N. (1984), Kinetic concept of the strength of solids, *Int. J. Fract. Mech.* **26**, 4, 295-307, DOI: 10.1007/BF00962961.

Zhurkov, S.N., V.S. Kuksenko, V.A. Petrov, V.N. Savelev, and U.S. Sultanov (1980), Concentration criterion of rock volume fracture. **In**: *Physical Processes in Earthquake Sources*, Nauka, Moscow, 78-86 (in Russian).

Utsu, T. (2002), Statistical features of seismicity. **In:** W.H.K. Lee, H. Kanamori, P.C. Jennings, and C. Kisslinger (eds.), *International Handbook of Earthquake and Engineering Seismology*, Part A, Academic Press, San Diego, 719-732, DOI: 10.1016/S0074-6142(02)80246-7.

Utsu, T., Y. Ogata, and R.S. Matsu'ura (1995), The centenary of the Omori formula for decay law of afterschock activity, *J. Phys. Earth* **43**, 1-33, DOI: 10.4294/jpe1952.43.1.

Received 14 May 2013
Received in revised form 18 November 2013
Accepted 27 November 2013